

Neutral strangeness production with the ATLAS detector at the Large Hadron Collider

Erny Au Yang

Department of Physics McGill University, Montréal

September, 2024

A thesis submitted to McGill University in partial fulfillment of the requirements of the degree of

Master of Science

© Erny Au Yang, 2024

Abstract

The strange quark is the lightest sea quark in the proton after the up and down quarks, and its production in pp collisions reveals some of the internal proton structure, the fragmentation processes of the proton and improves our understanding of soft QCD processes. In this work, the production of neutral strange hadrons, specifically K_s^0 , Λ^0 and $\bar{\Lambda}^0$, is studied using minimum-bias data from pp collisions at $\sqrt{s}=13$ TeV recorded by the ATLAS detector at the LHC. The kinematic distributions and multiplicities of these particles are presented and compared with predictions from Monte Carlos, where clear discrepancies are observed in certain distributions. Reconstruction efficiencies are estimated using Monte Carlo samples, leading to differential production cross section measurements.

Résumé

Le quark étrange est le quark de la mer le plus léger du proton après les quarks up et down, et sa production dans les collisions pp révèle une partie de la structure interne et les processus de fragmentation du proton et améliore notre compréhension des processus de QCD à basses énergies. Dans ce travail, la production de hadrons étranges neutres, en particulier K_s^0 , Λ^0 et $\bar{\Lambda}^0$, est étudiée en utilisant les données de biais minimum des collisions pp à $\sqrt{s}=13$ TeV enregistrées par le détecteur ATLAS au LHC. Les distributions cinématiques et les multiplicités de ces particules sont présentées et comparées aux prédictions de Monte Carlos, où des divergences claires sont observées dans certaines distributions. Les efficacités de reconstruction sont estimées à l'aide d'échantillons de Monte Carlo, ce qui mère à des mesures de sections efficaces différentielles de production.

Table of Contents

A	bstra	ct		i
Acknowledgements Contribution of authors			vi vii	
Li	st of	Tables	5	xi
1	Intr	oducti	ion	1
2	The	ory		3
	2.1	The S	tandard Model of particle physics	3
		2.1.1	Particle content and interactions	3
		2.1.2	Limitations of the Standard Model	5
	2.2	Quant	um chromodynamics and proton structure	5
		2.2.1	Parton distribution functions	7
	2.3	Physic	es of proton-proton collisions	8
		2.3.1	Hadronization	9
		2.3.2	Diffractive physics	9
	2.4	Strang	geness production	11

TABLE OF CONTENTS

3	Experimental setup		
	3.1	The Large Hadron Collider	13
3.2 The ATLAS detector		The ATLAS detector	16
		3.2.1 Coordinate system	16
		3.2.2 Magnet system	17
		3.2.3 Inner Detector	18
		3.2.4 Calorimeters	20
		3.2.5 Muon Spectrometer	22
	3.3	Trigger system	25
		3.3.1 Minimum Bias Trigger	25
4	Dat	a and Monte Carlo samples	27
	4.1	Data samples	27
	4.2	Monte Carlo samples	27
5	Sele	ection of K^0_s and $\Lambda^0(\bar{\Lambda^0})$ candidates	30
	5.1	Event selection	30
	5.2	V^0 reconstruction	30
	5.3	V^0 candidate selection	32
	5.4	Mass distributions	33
	5.5	Lifetime distributions	38
6	Res	ults for K^0_s and $\Lambda^0(ar{\Lambda^0})$	41
	6.1	Kinematic distributions	41
	6.2	Multiplicity distributions	42
	6.3	Reconstruction efficiencies	42
	6.4	Cross section measurements	43

TABLE OF CONTENTS

7 Conclusion and outlook	56
List of Abbreviations	58
References	60

Acknowledgements

First of all, I would like to express my sincere gratitude to my supervisor, Prof. François Corriveau, for providing me with the opportunity to work on this analysis and for his guidance along the way. I cannot thank him enough for his patience and encouragement. I would also like to thank Dr. Raphaël Hulsken deeply for his help with various technical issues and valuable advice on research in general. Many thanks to Prof. Brigitte Vachon and Prof. Andreas Warburton for their suggestions and discussions on analysis methods. I am also very grateful for the help I received from different members of the ATLAS-McGill group, past and present, who were very welcoming and very willing to help me get started.

I am also grateful to my friends in Montreal and around the world for their support and motivation. Finally and most importantly, the thesis would not have been possible without my parents, who had always believed in and supported me unconditionally.

Contribution of authors

The overview of the theory and the description of the ATLAS detector and samples used are written by the author. The subsequent chapters describe the analysis methods and results, which are the author's own work.

The data used in this analysis is collected using the ATLAS detector, the operation of which is a collaborative effort from thousands of members around the world. The analysis uses a V^0 reconstruction algorithm, which is part of an analysis framework developed by the members of the collaboration.

List of Figures

2.1	Elementary particles of the Standard Model and their properties, including	
	the three generations of quarks and leptons, the gauge bosons and the Higgs	
	boson [3]	4
2.2	Summarized values of the strong coupling constant α_S at different energy	
	scales Q , determined from various experiments [10]	6
2.3	An example set of proton PDFs at two different energy scales (Q^2) , where	
	$f(x,Q^2)$ represents the probability density of finding a parton carrying mo-	
	mentum fraction x [15]	8
2.4	Diagrams for (a) non-diffractive, (b) single-diffractive, (c) double-diffractive	
	and (d) central-diffractive processes in pp collisions. Here, diffractive processes	
	are mediated by Pomeron exchange. [23]	10
2.5	Rapidity distributions of final state hadrons in (a) non-diffractive, (b) single-	
	diffractive, (c) double-diffractive and (d) central-diffractive processes in pp	
	collisions. The thin vertical lines represent the scattered protons, typically in	
	the very forward rapidity regions. $[24]$	11
3.1	Schematic diagram of the CERN accelerator complex, as of 2022 [27]	15
3.2	Cut-away diagram of the ATLAS detector [28]	16
3.3	Simplified schematic diagram of the ATLAS magnet system [36, 37]	18

3.4	Cut-away diagram of the ATLAS inner detector, with distances from the	
	beamline shown [38]	19
3.5	Cut-away diagram of the ATLAS calorimeter system [28]	21
3.6	Cut-away diagram of the ATLAS muon spectrometer [28]	23
3.7	Schematic diagram of the newly installed NSWs in the ATLAS detector [43]	24
5.1	V^0 decay schematics	32
5.2	The distribution of V^0 candidates with respect to (a) $cos\theta$, (b) R_{xy} and (c)	
	p_T . The vertical lines in magenta and red show the minimum cuts used to	
	select K^0_s and $\Lambda^0(\bar{\Lambda^0})$ candidates, respectively	34
5.3	2D histogram of reconstructed K_s^0 mass and Λ^0 mass. The lines and arrows	
	in red (magenta) show cuts on the reconstructed K^0_s (Λ^0) mass to select Λ^0	
	(K_s^0) candidates	35
5.4	Mass distributions of (a) K_s^0 , (b) Λ^0 and (c) $\bar{\Lambda^0}$ candidates in data, fitted with	
	a Gaussian, double Gaussian, or non-relativistic Breit-Wigner signal on a 2nd	
	order polynomial background	36
5.5	Lifetime distributions of (a) K_s^0 and (b) Λ^0 candidates in data, fitted with the	
	signal plus background function described in Section 5.5	40
6.1	Distributions of (a) K_s^0 and (b) Λ^0 invariant masses in data and MC, with	
	fitting performed on data as shown by the solid red line. MC histograms are	
	normalized to data in the signal region, which is indicated by pairs of solid	
	magenta lines	45
6.2	Kinematic distributions of K_s^0 candidates in data and MC with respect to (a)	
	p_T , (b) η and (c) ϕ .MC histograms are normalized to data	46
6.3	Kinematic distributions of Λ^0 candidates in data and MC with respect to (a)	
	p_T , (b) η and (c) ϕ .MC histograms are normalized to data	47

6.4	Kinematic distributions of K_s^0 candidates in data and the non-diffractive (ND),	
	single diffractive (SD) and double diffractive (DD) subsamples from PYTHIA	
	8, with respect to (a) p_T , (b) η and (c) ϕ . The PYTHIA 8 subsample histograms	
	are separately normalized to data	48
6.5	Kinematic distributions of Λ^0 candidates in data and the non-diffractive (ND),	
	single diffractive (SD) and double diffractive (DD) subsamples from PYTHIA	
	8, with respect to (a) p_T , (b) η and (c) ϕ . The PYTHIA 8 subsample histograms	
	are separately normalized to data	49
6.6	$\bar{\Lambda^0}/\Lambda^0$ production ratios in data and MC with respect to (a) p_T , (b) η and (c)	
	ϕ . Only statistical uncertainties are shown	50
6.7	Particle multiplicity distributions of (a) K^0_s , (b) Λ^0 and (c) $\bar{\Lambda^0}$ in data and	
	MC, normalized to unity	51
6.8	Reconstruction efficiencies of K_s^0 from the two MC models used, with respect	
	to (a) p_T , (b) η and (c) ϕ . Only truth K_s^0 's decaying via $K_s^0 \to \pi^+\pi^-$ are	
	considered. Only statistical uncertainties are shown	52
6.9	Reconstruction efficiencies of Λ^0 from the two MC models used, with respect	
	to (a) p_T , (b) η and (c) ϕ . Only truth Λ^0 's decaying via $\Lambda^0 \to p\pi^-$ are	
	considered. Only statistical uncertainties are shown	53
6.10	Reconstruction efficiencies of $\bar{\Lambda^0}$ from the two MC models used, with respect	
	to (a) p_T , (b) η and (c) ϕ . Only truth $\bar{\Lambda^0}$'s decaying via $\bar{\Lambda^0} \to \bar{p}\pi^+$ are	
	considered. Only statistical uncertainties are shown	54
6.11	Differential production cross section for K^0_s, Λ^0 and $\bar{\Lambda^0}$ in arbitrary units, with	
	respect to (a) p_T , (b) η and (c) ϕ . Only statistical uncertainties are shown.	55

List of Tables

4.1	Weights applied to the Pythia 8 ND, SD and DD samples such that the	
	ratios between the weighted number of events match their relative inclusive	
	cross sections	29
5.1	Cut flow for data events	31
5.2	Cut flow for MC events	31
5.3	Selection cuts on V^0 candidates	33
5.4	Fit parameters to mass distributions in data. For the double Gaussian fit,	
	C_1/C_2 is the ratio between the amplitudes of the two Gaussians	37
5.5	Comparisons between fitted and Particle Data Group (PDG) mass values [63].	
	The fitted values for K_s^0 are obtained from the double gaussian fit, and for Λ^0	
	and $\bar{\Lambda^0}$ from the Breit-Wigner fit.	38
5.6	Fit results to lifetime distributions compared to the known mean lifetime	
	values from Particle Data Group (PDG) [63]	39

Chapter 1

Introduction

The Standard Model of particle physics is a gauge quantum field theory describing all known particles and the interactions between them, including the strong, weak and electromagnetic interactions, and is widely considered a successful theory as it is capable of predicting certain particle phenomena with great precision. However, it is not a complete model as it does not incorporate gravity and fails to explain various physical problems, such as the nature of dark matter, neutrino mass, and matter-antimatter asymmetry in the universe, amongst others.

In addition, quantum chromodynamics (QCD), which is the theory describing the strong interaction between quarks and gluons, is not well understood. While perturbative techniques are widely used in different physical scenarios, such as the electroweak sector, it cannot be employed in soft QCD. This is because of the fundamental nature of the strong coupling constant, which increases at lower energy scales and quickly diverges on the order of 100 MeV. On this energy scale, one must turn to phenomenological models, which depend on sets of input parameters that can only be tuned using experimental observations.

The proton and the neutron, which make up the nuclei of atoms found in everyday matter, are known to have internal structures. The proton in particular contains two up quarks and one down quark, known as valence quarks, with a sea of other quark-antiquark pairs and

gluons. It is non-trivial how heavier quarks are produced and present in the final states of proton-proton (pp) collisions as it requires many assumptions on the internal structure of the proton and how hadrons are created from scattered partons, in a process known as hadronization. In particular, the production of the strange quark, whose mass is around the divergence scale of QCD, is not well understood as it falls into the non-perturbative regime. Hence, by studying the production of strange hadrons from pp collisions, certain parameters in phenomenological models can be constrained, which leads to a better understanding of hadronization, parton interactions, and the complex internal structure of the proton.

In this work, the production of neutral strange hadrons, K_s^0 , Λ^0 and $\bar{\Lambda^0}$, from pp collisions at $\sqrt{s}=13$ TeV in the ATLAS detector, is studied. A total of 13.65 nb⁻¹ of minimum bias data is used, along with two Monte Carlo (MC) samples generated from different phenomenological models. Comparisons between data and MC are made for the strange hadron kinematic distributions and multiplicities. Using the reconstruction efficiencies obtained from the MC samples, the production differential cross sections are presented.

This thesis starts with a brief overview of the Standard Model and the various aspects of a pp collision in Chapter 2, followed by a short description of the ATLAS detector in Chapter 3 and the data and MC samples in Chapter 4. The reconstruction and selection of strange hadron candidates are detailed in Chapter 5, and the kinematic distributions, multiplicities, reconstruction efficiencies and differential cross section measurements are presented in Chapter 6. A conclusion and outlook of the analysis are provided in Chapter 7.

Chapter 2

Theory

2.1 The Standard Model of particle physics

The Standard Model (SM) of particle physics is a very successful theory describing the known particles in our universe and how they interact with each other under the electroweak and strong interactions, but, as mentioned in the introduction, it remains incomplete. It contains spin- $\frac{1}{2}$ fermions that make up all known matter, spin-1 gauge bosons that mediate the strong, weak and electromagnetic interactions, and since 2012 a spin-0 Higgs boson. Their basic properties are also shown in Figure 2.1. A brief introduction of the SM is given below, and the reader is referred to [1] and [2] for a more detailed description.

2.1.1 Particle content and interactions

The SM is a quantum field theory with gauge symmetry group $SU(3) \times SU(2) \times U(1)$, where particle interactions are mediated by the spin-1 gauge bosons. The SU(3) symmetry corresponds to the eight gluons that mediate the strong interaction between particles that carry the colour charge, i.e. quarks and gluons. The $SU(2) \times U(1)$ group corresponds to the four electroweak bosons, including the W^+ , W^- and Z bosons that mediate weak

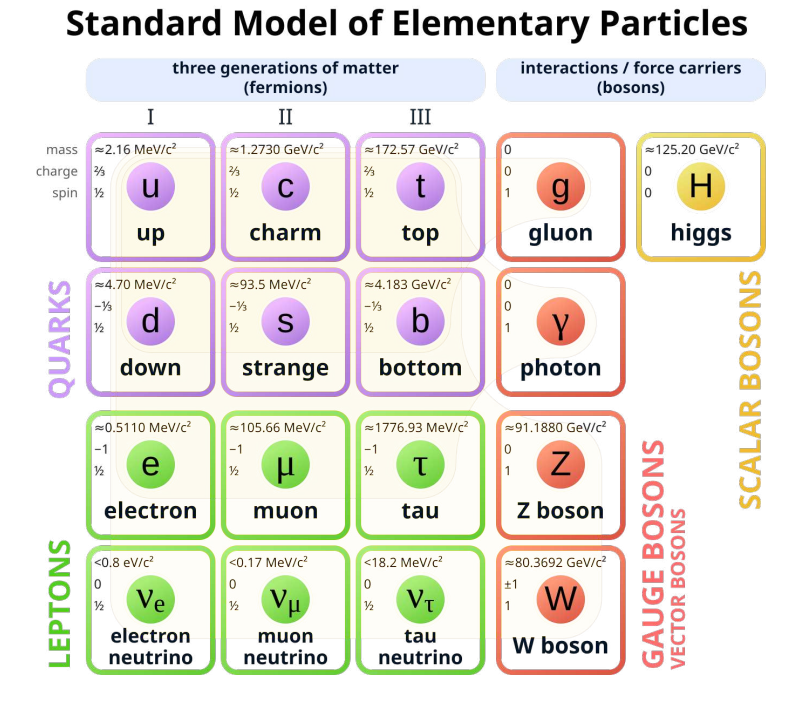


Figure 2.1: Elementary particles of the Standard Model and their properties, including the three generations of quarks and leptons, the gauge bosons and the Higgs boson [3].

interactions, and the photon (γ) that mediates electromagnetic interactions between particles that carry electrical charge.

The Higgs boson, discovered in 2012 by ATLAS [4] and CMS [5], is a scalar boson associated with the Higgs field that gives mass to the W^+ , W^- and Z bosons and fermions. The gluon and photon are massless.

The fermions in the SM can be categorized as quarks and leptons, and are divided into three generations of increasing masses (except neutrinos). The three generations of leptons are electron (e^-) , muon (μ^-) and tau (τ^-) , and their respective associated neutrinos (ν_e, ν_μ) and ν_τ . The charged leptons interact via the electromagnetic and weak interactions, while the neutrinos only interact via the weak interaction in the SM.

The quarks come in six different flavors, namely up, down, charm, strange, top and bottom (u, d, c, s, t and b respectively), and carry fractional electrical charges of either

 $+\frac{2}{3}e$ or $-\frac{1}{3}e$. They interact through strong, electromagnetic and weak interactions. In the SM, quark flavor can only be changed via charged weak interactions (i.e. by exchanging a W^{\pm}), with the coupling between different flavors described by the CKM matrix [6]. Quarks cannot exist freely due to the asymptotic freedom of quantum chromodynamics, which will be discussed further in Section 2.2.

For each fermion, there exists a corresponding antiparticle with the same mass but opposite quantum numbers.

2.1.2 Limitations of the Standard Model

The SM is a very successful theory as it describes many aspects of nature with great precision, but it is far from a theory of everything. The most obvious shortcoming lies in the exclusion of gravity, which does not have a quantum mechanical interpretation.

Another shortcoming of the SM is the failure to explain dark matter and dark energy, which have been proven to exist by various experiments and observations, and constitute the majority of mass-energy in the universe [7]. The fact that our universe is mostly matter, known as matter-antimatter asymmetry, is also unaccounted for by the SM as it predicts that matter and antimatter were created in equal amounts during the early universe [8].

Moreover, the SM predicts that neutrinos are massless, yet the observation of neutrino oscillations, which can only proceed if different flavored neutrinos have different masses, imply that neutrinos must have non-zero masses [9].

2.2 Quantum chromodynamics and proton structure

Quantum chromodynamics (QCD) is the theory describing strong interactions, which are interactions between particles with colour charge, namely quarks and gluons. The underlying group, SU(3), has eight generators, which correspond to the eight gluons, and three

orthogonal states, which correspond to the three colours, conventionally denoted red, green and blue. Each (anti)quark carries a (anti)colour, and a colourless bound state can be created with three (anti)quarks each carrying a different (anti)colour, forming a (anti)baryon, or with a quark-antiquark pair carrying the same colour-anticolour, forming a meson.

One unique feature of QCD is its asymptotic freedom, which refers to the fact that the strong coupling constant (α_S) increases with decreasing energy scale (Q) as shown in Figure 2.2. Equivalently, α_S increases with distance because the interaction length scale r follows the relation $r \sim 1/Q$, which implies that the energy required to separate quarks in a colourless bound state would increase with separation and become so large at some point that quark-antiquark pairs are created from the vacuum. Hence, single quarks, which are coloured, cannot exist freely, and quarks are only stable in colourless states, also known as colour confinement.

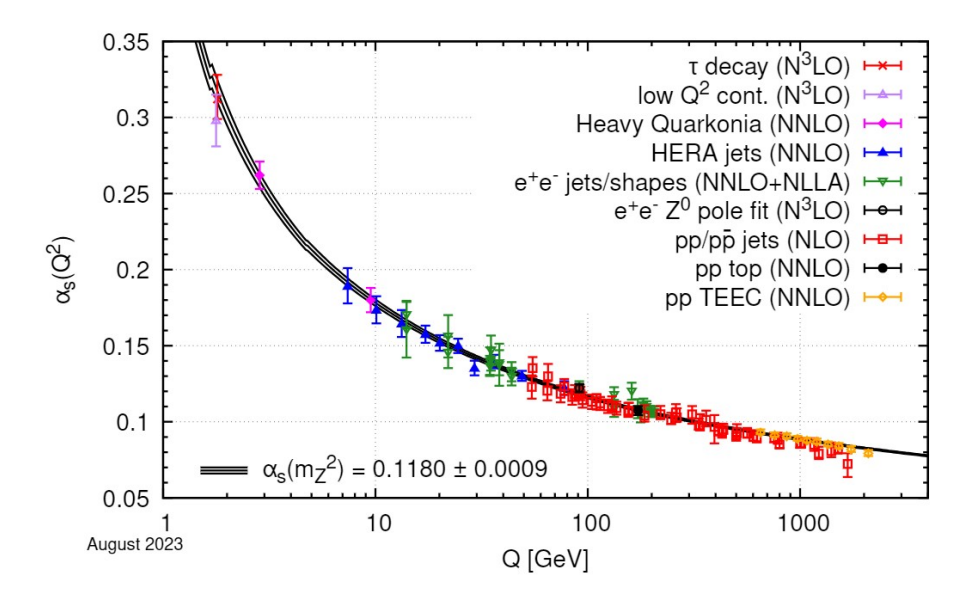


Figure 2.2: Summarized values of the strong coupling constant α_S at different energy scales Q, determined from various experiments [10].

Another consequence of asymptotic freedom is that perturbative techniques fail at low energy scales, which means that perturbative QCD cannot be used to accurately model soft processes, such as the creation of strange hadrons from hadronic collisions, which have low p_T . Phenomenological models with many input parameters have to be employed, and the tuning of these parameters relies on experimental data.

One non-perturbative approach is Lattice QCD, which discretizes spacetime into a lattice, with quark fields placed on the lattice sites and gluon fields represented by links between the sites [10, 11]. Lattice QCD is a rapidly developing field that has made various successful predictions, such as the masses of light hadrons with percent-level accuracy [12].

2.2.1 Parton distribution functions

An example of a colourless bound state of three quarks is the proton, which is made up of two up and one down quarks, also known as the valence quarks. The proton is stable as it is the lightest baryon and hence does not decay due to conservation of baryon number. The picture that a proton only contains the *uud* quarks is incomplete, as deep inelastic scattering experiments (e.g. *ep* collisions) reveal that the proton also contains gluons and many quark-antiquark pairs, known as sea quarks [13]. Collectively, the constituents of the proton are called partons.

The structure of the proton can be described using parton distribution functions (PDFs), denoted $f_i(x, Q^2)$, which represent the probability density to find a parton i in the proton carrying a fraction x of the total momentum of the proton. The PDF is also dependent on the momentum exchanged squared in the scattering process, Q^2 . An example set of PDFs at two Q^2 values is shown in Figure 2.3, where the ordinate of the plots is $xf(x,Q^2)$ and the abscissa is x, and the area under a curve can be interpreted as the total momentum fraction carried by partons of that specific type. The plots exhibit some general features of PDFs, including:

- at fixed Q^2 , sea quarks and gluons dominate at small x;
- at small x, the sea quarks and gluon densities increase with Q^2 ;

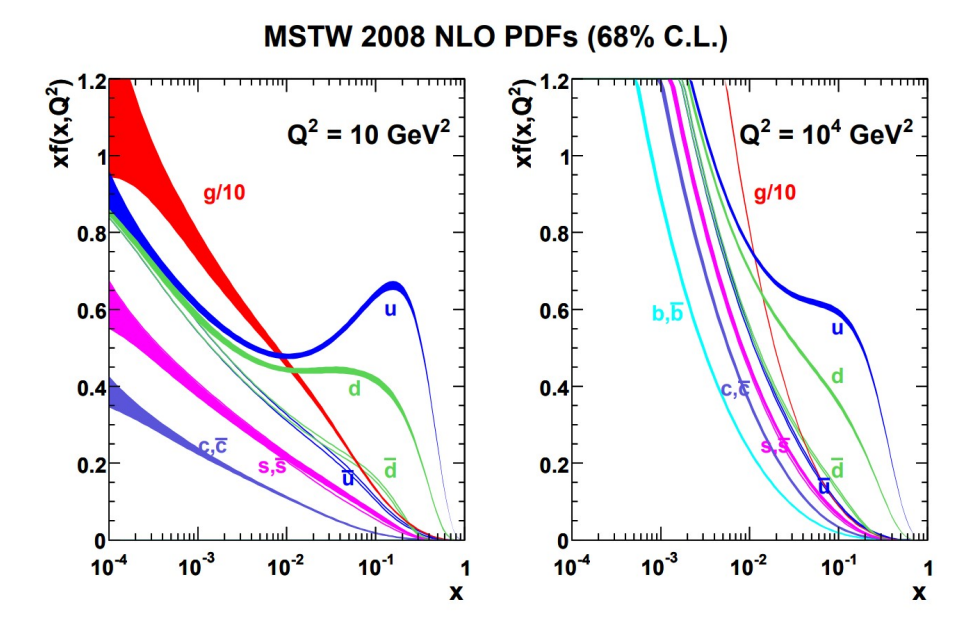


Figure 2.3: An example set of proton PDFs at two different energy scales (Q^2) , where $f(x, Q^2)$ represents the probability density of finding a parton carrying momentum fraction x [15].

 \bullet gluons dominate at small x in general.

While the evolution of PDFs with Q^2 can be described analytically, the determination of PDFs at a particular Q^2 value cannot be obtained from first principle calculations and relies solely on experimental data [14].

2.3 Physics of proton-proton collisions

The total proton-proton (pp) cross section can be broken down into elastic and inelastic components. As protons remain intact and no new particles are created in elastic collisions, we focus our discussion on inelastic collisions, where interesting physics is found. The pp collision itself can be separated into hard and soft interactions, which refer to processes with high and low momentum transfer, respectively. Hard processes can be modelled by perturbative techniques, whereas soft processes are much less understood. In this section, a brief overview is given on some aspects of inelastic pp collisions.

2.3.1 Hadronization

In inelastic pp collisions, partons from each proton may undergo scattering and are freed from the bound state. Due to colour confinement, the scattered partons will hadronize, forming a collimated spray of hadrons, known as a jet. In a particle detector, jets are measured and the type and momentum of the initial state parton could in principle be inferred.

Hadronization is a complicated process that is not fully understood, and cannot be calculated from first principles. It is usually described by fragmentation functions $D_i^h(z)$, which can be interpreted as the probability of an initial state parton i hadronizing into a final state hadron h carrying a fraction z of the parton's momentum. Fragmentation functions are said to be universal as they are the same in different processes with hadrons in the final state, such as in e^+e^- , ep and pp collisions [16]. Consequently, one must consider the experimental data from all these processes when tuning fragmentation function parameters [10].

One of the hadronization models is the Lund string fragmentation model [17], where the strong force, or colour field between partons, is represented by strings, and quark-antiquark pairs are created when these strings break, leading to hadronization. Pythia is an event generator that handles hadronization using only this model [18].

2.3.2 Diffractive physics

The total inelastic pp cross section can be broken down into non-diffractive (ND) and diffractive components, with the latter further broken down into single diffractive (SD), double diffractive (DD) and other processes such as central diffractive (CD), as illustrated in Figure 2.4 and described by the equation:

$$\sigma_{inel} = \sigma_{ND} + \sigma_{SD} + \sigma_{DD} + \sigma_{misc} \tag{2.1}$$

ND processes are when hadrons are created from the exchange of colour charge between

the two protons, and are the dominant contributions to the total pp cross section at Large Hadron Collider (LHC) energies [19]. In contrast, diffractive processes occur when no quantum numbers are exchanged between the colliding protons.

Diffractive processes contribute to the soft part of the hadronic interaction. One possible description of diffractive processes involves the exchange of Pomerons [20], which are colour-singlet particles with quantum numbers of the vacuum that were theorized to explain the slow increase of total hadron-hadron cross sections at high energy [21]. In this picture, SD and DD processes refer to the dissociation of one and two protons respectively involving the exchange of one pomeron, while in the CD scenario the two protons remain intact and two Pomerons are exchanged. At LHC energies we have $\sigma_{SD} > \sigma_{DD} > \sigma_{CD}$ [19].

Measurements of cross sections of diffractive processes are crucial to understanding *pp* collisions and provide another way of tuning parameters in phenomonological models [22]. In principle, diffractive events can be selected using their large rapidity gaps, i.e. rapidity regions where no final state hadrons are found. The rapidity distributions of final state hadrons of various processes are shown in Figure 2.5.

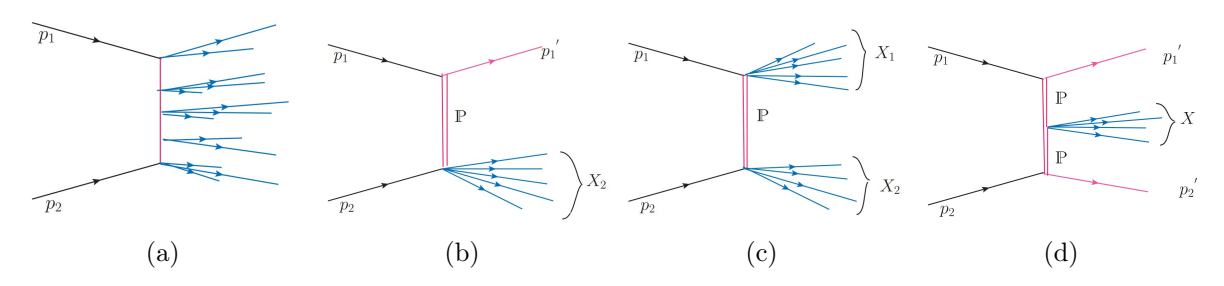


Figure 2.4: Diagrams for (a) non-diffractive, (b) single-diffractive, (c) double-diffractive and (d) central-diffractive processes in pp collisions. Here, diffractive processes are mediated by Pomeron exchange. [23]

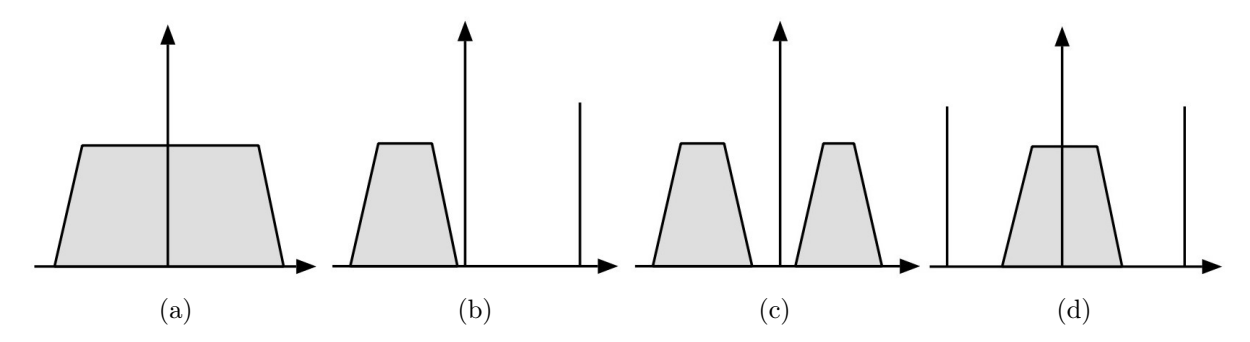


Figure 2.5: Rapidity distributions of final state hadrons in (a) non-diffractive, (b) single-diffractive, (c) double-diffractive and (d) central-diffractive processes in pp collisions. The thin vertical lines represent the scattered protons, typically in the very forward rapidity regions. [24]

2.4 Strangeness production

The strange quark is not a valence quark of the proton, but because of its low mass compared to LHC energies, it is produced in abundance in pp collisions. Strangeness production occurs in both the hard and soft parts of the pp collisions, which are mainly responsible for the production of strange hadrons with high and low p_T , respectively [25]. The empirical observation that most strange hadrons have low p_T hence implies that soft, non-perturbative QCD is crucial to strangeness production, which requires phenomenological models whose parameters must be tuned using experimental data.

One of the strangeness production mechanisms is that strings fragment into a strangeantistrange pair, which is obviously suppressed compared to fragmentation into up or down quark-antiquark pairs due to mass differences [25]. The level of suppression, which directly affects multiplicities of strange hadrons, is dictated by a set of string fragmentation parameters in each model.

In this work, the production of neutral, singly stranged hadrons K_s^0 and $\Lambda^0(\bar{\Lambda^0})$ is studied. Their kinematic distributions and multiplicities measured using the ATLAS detector are compared with predictions from two Monte Carlo samples that are created based on dif-

ferent phenomenological models. Although the actual tuning of model parameters is beyond the scope of this analysis, the qualitative differences between each model predictions and experimental data can help refine future simulations.

Chapter 3

Experimental setup

The data used in this analysis are recorded by the ATLAS detector, which is one of the detectors in the LHC. In this chapter a brief overview of the LHC and the components of the ATLAS detector is presented.

3.1 The Large Hadron Collider

The LHC is the most powerful and largest particle collider to date. It has a circumference of 27 km and is located underground at a mean depth of 100 m near Geneva, and is designed to collide protons at a maximum center-of-mass energy of 14 TeV and lead (Pb) ions at 2.8 TeV per nucleon [26]. Located within the CERN accelerator complex (Figure 3.1), it is injected with particles that passed through a series of accelerators: for protons, the energy is increased in steps by the Linear accelerator 4 (Linac4), then the Proton Synchrotron Booster (PSB), the Proton Synchrotron (PS), and the Super Proton Synchrotron (SPS) before finally entering the LHC beam pipes in bunches [27]. The particles are then further accelerated and bunched up by electric fields controlled by a Radio Frequency (RF) system, and particle beams are squeezed near interaction points by superconducting magnets in order to increase the probability of collision.

During pp runs, two beams of protons grouped in bunches circulate in opposite directions at a frequency of 40 MHz, which corresponds to a bunch spacing of 25 ns, and are set to collide at four interaction points where the major experiments are located. They include the ATLAS [28] and CMS experiments [29], which are both general purpose particle detectors with near full solid angle coverage, the LHCb detector [30] which specialises in physics of bottom-quark hadrons (B-physics), and the ALICE experiment [31] which specializes in physics of quark-gluon plasma and heavy-ion collisions.

An important quantity used to assess the performance of a particle collider is luminosity (\mathcal{L}) , defined by

$$\mathcal{L}(t) = \frac{1}{\sigma} \frac{dN}{dt} \tag{3.1}$$

where, in the context of pp collisions at the LHC, $\frac{dN}{dt}$ is the number of pp interactions per unit of time and σ is the pp cross section.

The integrated luminosity is given by

$$\mathcal{L}_{int} = \int \mathcal{L}(t) dt = \frac{1}{\sigma} \cdot N$$
 (3.2)

and quantifies the amount of data collected over a period of time.

The LHC operates during different Runs, separated by Long Shutdowns for technical upgrades and maintenance, with increasing collision energy and luminosity. Run 1 (2009-2013) saw pp collisions at up to center-of-mass energy $\sqrt{s} = 8$ TeV [32], which then increased in Run 2 (2015-2018) to $\sqrt{s} = 13$ TeV [33]. Run 3 began in 2022 and has seen a maximum of $\sqrt{s} = 13.6$ TeV [34]. The High Luminosity LHC phase, expected to begin in 2029, aims to reach instantaneous luminosity values of 5 times the original designed value of the LHC and will require significant upgrades in accelerator and detector hardware [35].

The CERN accelerator complex Complexe des accélérateurs du CERN **CMS** North LHC Area ALICE **LHCb** SPS **ATLAS** HiRadMat 2011 TT66 **MEDICIS ELENA** AD ISOLDE **BOOSTER** 1972 (157 m) **East Area** PS LINAC 4 HT 2020 CLEAR 2017 LEIR ▶ RIBs (Radioactive Ion Beams) ► H (hydrogen anions) ► p (protons) p (antiprotons) ions n (neutrons) LHC - Large Hadron Collider // SPS - Super Proton Synchrotron // PS - Proton Synchrotron // AD - Antiproton Decelerator // CLEAR - CERN Linear Electron Accelerator for Research // AWAKE - Advanced WAKefield Experiment // ISOLDE - Isotope Separator OnLine // REX/HIE-ISOLDE - Radioactive EXperiment/High Intensity and Energy ISOLDE // MEDICIS // LEIR - Low Energy Ion Ring // LINAC - LINear ACcelerator //

Figure 3.1: Schematic diagram of the CERN accelerator complex, as of 2022 [27].

n_TOF - Neutrons Time Of Flight // HiRadMat - High-Radiation to Materials // Neutrino Platform

15

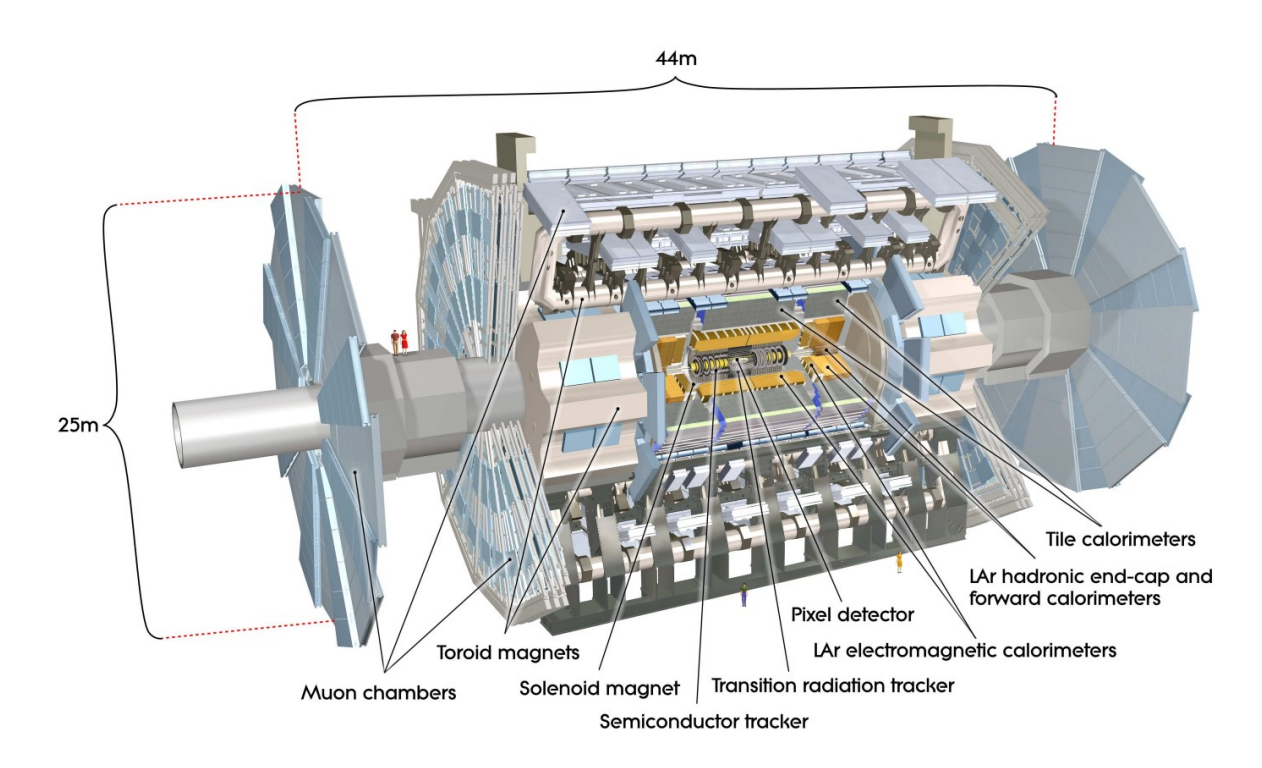


Figure 3.2: Cut-away diagram of the ATLAS detector [28].

3.2 The ATLAS detector

The ATLAS detector is a general purpose particle detector located at one of the collisions point of the LHC [28]. With a length of 46 m and diameter of 25 m, it is the largest detector ever built for a collider experiment. It has a cylindrical geometry with forward-backward symmetry, and has near 4π solid angle coverage. The detector components, consisting of a magnet system, the inner detector, calorimeters, and muon spectrometer, are shown in Figure 3.2 and are briefly described in this section.

3.2.1 Coordinate system

ATLAS uses a right-handed coordinate system with its origin at the nominal interaction point, the z-axis along the beampipe, the positive x-axis pointing towards the center of the LHC ring and the positive y-axis pointing upwards. The azimuthal angle ϕ and polar angle

 θ are defined as angles around and from the z-axis respectively. Furthermore, pseudorapidity η is defined by $\eta = -\ln \tan(\theta/2)$, and any vector on the x-y plane would have $\eta = 0$ while a vector approaching the $\pm z$ -axis would have $\eta \to \pm \infty$. Rapidity is defined by $y = \frac{1}{2} \ln \frac{E + p_z}{E - p_z}$ and is equivalent to pseudorapidity in the relativistic limit or if the particle is massless. The angular separation between two vectors is represented by $\Delta R = \sqrt{(\Delta \eta)^2 + (\Delta \phi)^2}$. Transverse physical quantities are defined in the x-y plane - for instance, transverse momentum p_T is the projection of the momentum vector on the x-y plane.

3.2.2 Magnet system

The magnet system in the ATLAS detector creates magnetic fields that bend the trajectories of charged particles and allow their momenta to be measured. As particles created at the LHC can have large momenta, strong field strengths are required to create sufficient curvature for better momentum measurements. This is achieved with four superconducting magnets [28, 36], as shown in Figure 3.3:

- the central solenoid, measuring 5.8 m in axial length and 2.56 m in diameter (outer), provides a 2 T axial field along the z-axis in the central tracking volume, i.e. the inner detector;
- the barrel toroid, measuring 25.3 m in axial length and 20.1 m in diameter (outer), is the largest toroidal magnet ever built and provides a toroidal field of up to 2.5 T in the central regions of the muon spectrometer;
- the two end-cap toroids, measuring 5.0 m in axial length and 10.7 m in diameter (outer), provides a toroidal field of up to 3.5 T in the end-cap regions of the muon spectrometer.

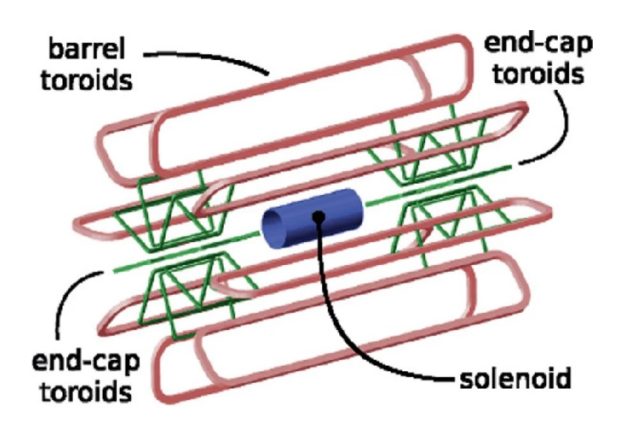


Figure 3.3: Simplified schematic diagram of the ATLAS magnet system [36, 37].

3.2.3 Inner Detector

The Inner Detector (ID), shown in Figure 3.4, is a tracking detector located closest to the beamline with a coverage of $|\eta| < 2.5$. It is capable of measuring the sign of charge and the momenta of charged particles with great precision by measuring the direction and radius of curvature of their tracks under the 2T magnetic field. It is also responsible for reconstructing the primary and secondary vertices of an event using charged particle tracks above the p_T thresholds of 0.5 GeV for nominal conditions and 0.1 GeV for minimum bias runs, which is explained in Section 3.3.1 [28, 39]. The ID consists of three sub-detectors, listed here from innermost to outermost:

- the pixel detector consists of three cylindrical barrel layers and three end-cap discs on each end made of silicon semiconductors, providing a maximum of three hits per track. The insertable B-layer (IBL) was installed before Run 2 as an additional layer between the innermost barrel layer of the pixel detector and the beamline to compensate for the effects of radiation damage on the pixel detector [38], and the total number of readout channels, or pixels, is approximately 92 million.
- the silicon microstrip detector (SCT), also made of silicon semiconductor, consists of four cylindrical barrel layers and nine end-cap discs on each end, providing between 4 to

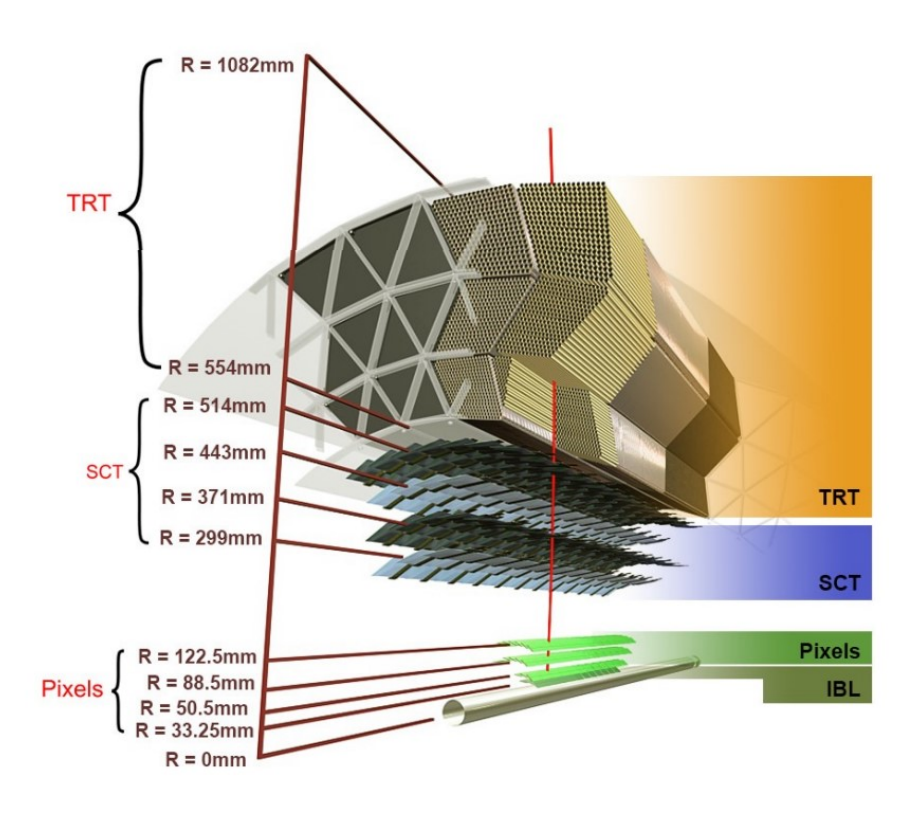


Figure 3.4: Cut-away diagram of the ATLAS inner detector, with distances from the beamline shown [38].

9 hits per track depending on the angle of trajectory, and has a total of approximately 6 million readout channels in the form of silicon microstrips.

• the transition radiation tracker (TRT) contains drift tubes, or "straws", with 73 layers in its barrel and 160 planes on each end-cap. Each straw is filled with a xenon-based gas mixture and has an anode wire in the center. When a charged particle passes through a straw, the gas mixture is ionized, and the ions drift to the anode wire and this is registered as a hit. In addition, the material between straws causes passing charged particles to emit transition radiation photons, which are detected by the straws and can be used to identify particles - primarily electrons due to its low mass which leads to more intense radiation. Although the TRT has poorer resolution per detector unit than the silicon detectors, it significantly enhances the precision of momentum measurements in the ID by providing long track measurements, averaging 36 hits per track.

3.2.4 Calorimeters

The calorimeter system of the ATLAS detector, shown in Figure 3.5, consists of sampling calorimeters with a coverage of $|\eta| < 4.9$ [28]. Sampling calorimeters contain layers of absorber material and active material, and the former turns an incoming particle into a cascade of secondary particles, or a shower, while the latter measures the energy deposited by the constituents of the shower. In the following, the two components of the calorimeter system are described: the electromagnetic calorimeters, which measure mostly the energy of electrons and photons, and the hadronic calorimeters, which measure mostly the energy of hadrons such as neutrons and pions.

• The electromagnetic component is handled by the liquid argon (LAr) electromagnetic calorimeter, which has a barrel and two end-cap sections providing an overall coverage

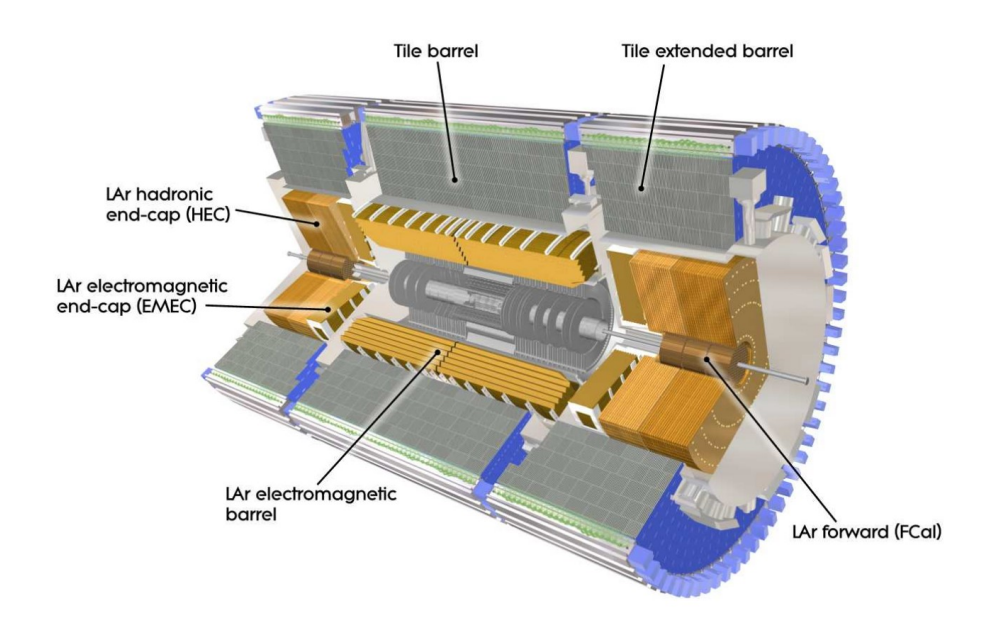


Figure 3.5: Cut-away diagram of the ATLAS calorimeter system [28].

of $|\eta| < 3.2$. Liquid argon, the active material, is filled between lead plates, the absorber material, in the calorimeter. As an incoming particle passes the lead plates, creating an electromagnetic shower, the argon is ionized and creates a current that is picked up by electrodes, which are arranged in an accordion shape to ensure minimal particle leakage and that the calorimeter is symmetric with respect to ϕ . The barrel and end-cap LAr calorimeters have a thickness of $22X_0$ and $24X_0$ respectively, where X_0 is the radiation length¹, providing effective containment of electromagnetic showers [40].

• The hadronic component is handled by three calorimeters. The first is the tile calorimeter, which has an overall coverage of $|\eta| < 1.7$ and uses plastic scintillators as active material and low-carbon steel plates as absorber material. As incoming particles create hadronic showers, the shower particles create scintillating light in the active layer, which is collected by wavelength-shifting fibres that are connected to photomultiplier

¹Radiation length is defined as the mean distance that an electron travels in a medium before its energy decreases by a factor of 1/e.

tubes, where the light intensity is measured and the energy of the shower particle is inferred. The tile calorimeter has a total thickness of $11\lambda_I$ at $\eta=0$, where λ_I is the nuclear interaction length², significantly reducing leakage of hadronic shower particles into the muon spectrometer [41]. The remaining two calorimeters are the LAr hadronic end-cap calorimeter and the LAr forward calorimeter. They cover $1.5 < |\eta| < 3.2$ and $3.1 < |\eta| < 4.9$, respectively, and have the same working principle as the electromagnetic calorimeter.

3.2.5 Muon Spectrometer

The muon is a charged lepton with a mass of about 200 times that of an electron. Its large mass prevents it from being contained by the electromagnetic calorimeters, as it undergoes minimal bremsstrahlung radiation and does not shower. As such, the Muon Spectrometer (MS), shown in Figure 3.6, makes up the outermost layer of the ATLAS detector and is dedicated to triggering, tracking and momentum measurement of muons with a total coverage of $|\eta| < 2.7$ [28]. The MS configuration during Run 2 consists of four detectors, described in the following:

- the monitored drift tube (MDT) chambers each consist of many drift tubes filled with a pressurized Ar-CO₂ gas mixture, stacked in three to eight layers per chamber. The gas is ionized when a charged particle passes through, then the ions drift under an electric potential and are collected at the central anode wire, creating a signal. There are three layers of MDT chambers in the barrel, and four layers on each end-cap, providing tracking and momentum measurement in the range of $|\eta| < 2.7$.
- the cathode-strip chambers (CSCs) is the innermost tracking component of the MS covering the end-cap region of $2.0 < |\eta| < 2.7$. It consists of multiwire proportional

²Nuclear interaction length is defined as the mean distance that a particle travels in a medium before undergoing an inelastic nuclear interaction.

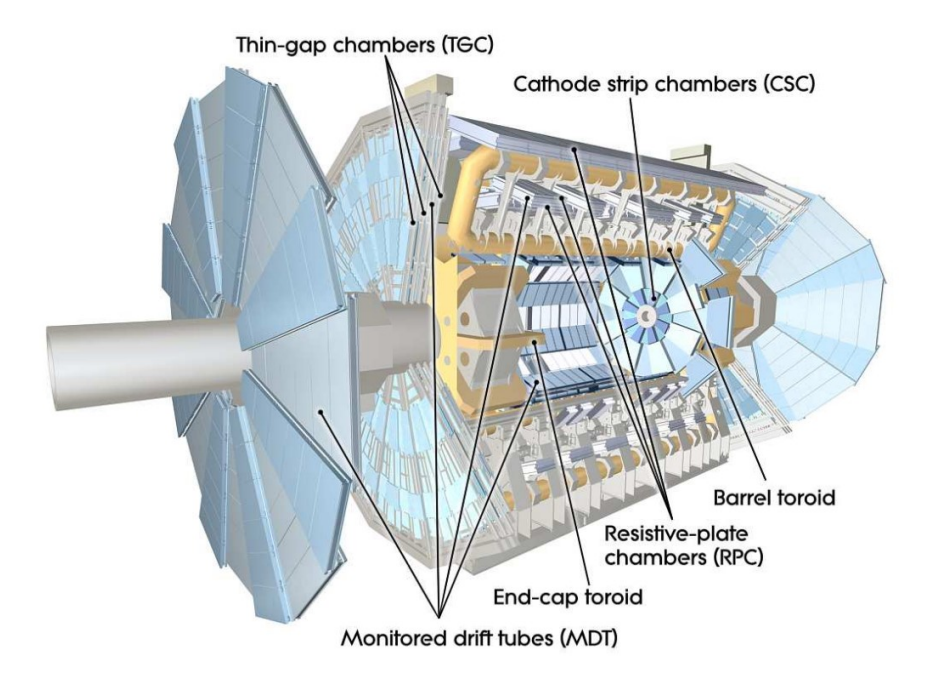


Figure 3.6: Cut-away diagram of the ATLAS muon spectrometer [28].

chambers filled with a Ar-CO₂ gas mixture, with a similar working principle as the MDT. Compared to the MDT however, the CSC has a much shorter electron drift time, making it suitable for the high muon flux environment in the forward region.

- the Resistive Plate Chambers (RPCs) make up the muon trigger system in the barrel region, with a coverage of $|\eta| < 1.05$. The RPC is a gaseous detector that consists of a set of parallel electrode plates with an electric field maintained in between. Despite its poor spatial resolution, its fast response time makes it ideal for triggering purposes.
- the Thin Gap Chambers (TGCs) is the other component of the muon trigger system, covering the end-cap region (1.05 $< |\eta| < 2.4$). They are multiwire proportional chambers with a high electric field and short distances between parallel wires, resulting in excellent timing resolution, which is critical to trigger systems.

Before the beginning of Run 3, the end-cap detectors were replaced by the New Small Wheels (NSWs) [42, 43, 44], with a coverage of $1.3 < |\eta| < 2.7$. Each NSW consists of

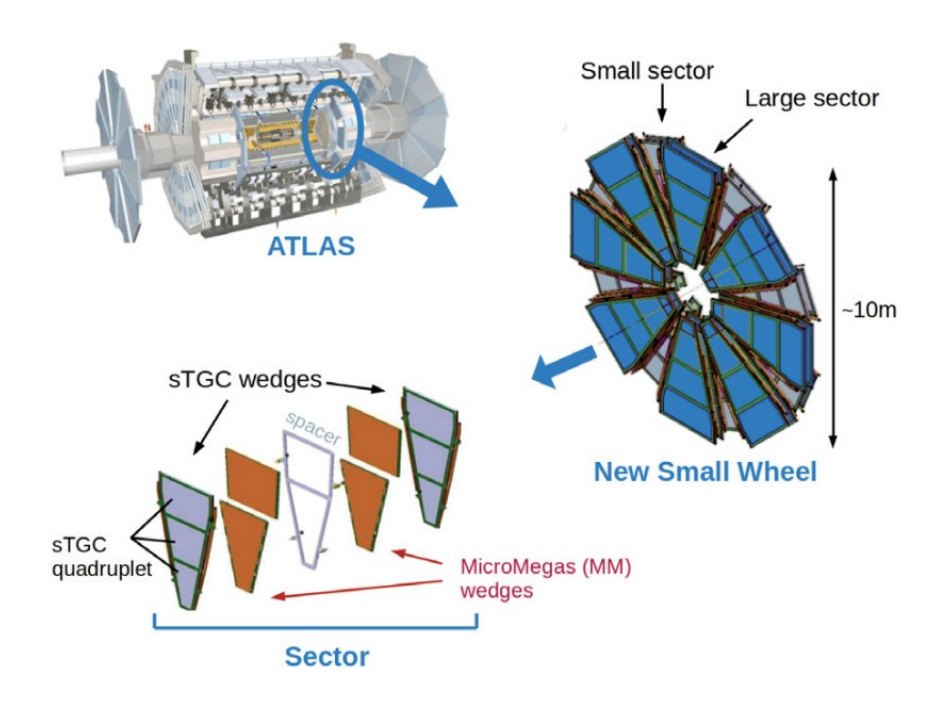


Figure 3.7: Schematic diagram of the newly installed NSWs in the ATLAS detector [43]

two new detector components, namely the small strips Thin Gap Chambers (sTGC) and Micromegas (MM), as shown in Figure 3.7. They are both gas-filled detectors responsible for both precision tracking and triggering, described in the following:

- the sTGC each consist of two cathode boards containing a gas gap filled with a $\rm CO_2+n$ Pentane gas mixture. They contain gold-coated tungsten wires that are subjected to
 an operational voltage of 2.8 kV in proportional mode.
- the MM detectors each consist of a planar electrode structure that is electrically divided by a metal micromesh into two gas volumes, namely the conversion/drift gap and amplification gap, filled with an Ar/CO₂/Isobutane gas mixture.

3.3 Trigger system

As mentioned in Section 3.1, the LHC has an event rate of 40 MHz, which makes it impossible to record every single event due to storage and bandwidth limitations. Triggers are hence required, which refer to systems implementing specific criteria to decide which events to keep or discard. Depending on the physics goals of a specific run, the trigger menu can be changed to select events with a different set of physical signatures; for instance, triggers that select events with large missing transverse energy are typically used in searches for new physics.

ATLAS uses a two-stage trigger system, which consists of the Level-1 (L1) trigger and the high level trigger (HLT) [45]. The L1 trigger is hardware-based, and uses reduced-granularity information from the calorimeter and muon spectrometer, such as total energy measured by the calorimeter of the number of muons above a certain p_T threshold, to quickly reduce the event rate to below 100 kHz. Typically, events with high- p_T objects and large missing p_T or E_T of enhanced physics interest are selected at this stage. L1 triggers also determine Region-of-Interest (ROI) in the $\eta - \phi$ plane in the detector, which are areas where certain criteria are met (such as p_T above some threshold), and pass this information to the HLT. The HLT is a software-based system that takes in high granularity information from all detectors within the ROI to perform fast reconstruction, allowing more refined selections to be made. The event rate is further reduced to 1.2 kHz on average after this stage.

3.3.1 Minimum Bias Trigger

As triggers used during nominal physics runs tend to favour events containing objects with large p_T or other physical quantities, they are intrinsically biased. However, in studies related to soft QCD processes, the key quantities, such as rapidity gap [46] and charge multiplicity [47], can only be measured accurately with as little bias as possible in the selection of events. This motivates the use of a minimum bias trigger during dedicated low luminosity periods

to record minimum bias data.

As part of the L1 trigger system, the minimum bias trigger utilises the Minimum Bias Trigger Scintillators (MBTS), which are polystyrene scintillator discs installed on the two ends of the ATLAS detector at approximately |z| = 3.6 m and cover the end-caps of the ID [48]. Each MBTS end-cap is made up of an outer $(2.08 < |\eta| < 2.76)$ and inner ring $(2.76 < |\eta| < 3.86)$, each segmented into 8 sections, allowing for up to 16 hits per end-cap. Minimum bias data is collected with a combination of minimum bias trigger settings, which, for example, require at least one or two hits in the MBTS, or at least one hit per end-cap of the MBTS, and has been shown to accept inelastic pp collision events with high efficiency and inclusiveness [49]. This is therefore the data used for this analysis.

Chapter 4

Data and Monte Carlo samples

4.1 Data samples

In this analysis, minimum bias data from pp collisions at $\sqrt{s} = 13$ TeV recorded in June 2015 (period B1) by the ATLAS detector are used. The sample consists of six special runs with low mean number of inelastic interactions per bunch-crossing $(\langle \mu \rangle)$, or low pile-up, with $\langle \mu \rangle$ of each run ranging between 0.003 and 0.03, which is drastically lower than the average of the 2015 dataset $(\langle \mu \rangle = 13.7)$ [50]. The data in these runs were recorded when the MBTS was triggered.

A Good Runs List (GRL)¹ is used to select events recorded when the detector components were functioning properly. The integrated luminosity of the data sample after passing GRL selections is $13.65 \pm 0.15 \text{ nb}^{-1}$ [51].

4.2 Monte Carlo samples

Monte Carlo (MC) simulations are commonly used in experimental particle physics for background estimation and detector response modelling. To prepare a MC sample, events are

 $^{^1} data 15_13 TeV. period B1_Det Status-v62-pro18_DQDefects-00-01-02_PHYS_Standard GRL_All_Goodeline Status-v62-pro18_DQDDefects-00-01-02_PHYS_Standard GRL_All_Goodeline Status-v62-pro18_DQDDefects-00-01-02_DQDDefects-00-01-02_DQDDefects-00-01-02_DQDDefects-00-01-02_DQDDefects-00-01-02_DQDDefects-00-01-02_DQDDefects-00-01-02_DQDDefects-00-01-$

first generated in free space following certain physical rules, which depend on the underlying theoretical model of the generator and the set of input parameters used, also known as "tune". The information created at this stage is commonly referred to as particle-level or truth-level. The detector response is then simulated and output as "hits" with the same format as data, which are then passed on to the reconstruction step where objects such as tracks and jets are created and saved to the final output.

As the preparation of MC samples is completely parallel to processes occurring in actual events, both MC and data samples can be analyzed in the same manner. In addition, truth-level information in MC samples enables the calculation of reconstruction efficiencies, which can then be used to perform unfolding on data to obtain the actual distribution of any variable of interest and make comparisons at particle level.

Two MC samples are used in this analysis. The first sample uses the EPOS generator [52, 53] with the EPOS-LHC tune [54], and the second uses PYTHIA 8 (version 8.186) inelastic [18] with the A2 tune [55], which is configured based on the MSTW2008LO PDF [15]. The two generators are based on different models that handle parton interactions and hadronization differently. The ATLAS detector response for both samples was simulated using GEANT4 [56, 57].

The EPOS generator is based on the parton-based Gribov-Regge theory [58], which is an effective field theory with QCD concepts in which partons interact via Pomeron exchange. The EPOS version used in this analysis features a core-corona model [54] where string hadronization is handled differently in the "core" and "corona", defined as regions with high and low colour string densities. Overall, EPOS models hard and soft scattering simultaneously, and is specifically designed to describe complete minimum bias events.

The PYTHIA 8 generator uses separate modelling for non-diffractive and diffractive processes. The former is mostly generated with gluon exchange between partons while the latter with colour-singlet exchange. Hadronization is based solely on the Lund string fragmentaion

	Number of events	Weights	Weighted number of events	Cross section [mb]
ND	19×10^{6}	1.000	19.00×10^6	56.79
SD	2×10^{6}	2.146	4.292×10^{6}	12.83
DD	2×10^{6}	1.472	2.944×10^{6}	8.80

Table 4.1: Weights applied to the PYTHIA 8 ND, SD and DD samples such that the ratios between the weighted number of events match their relative inclusive cross sections.

models. Multiple parton interaction is possible in Pythia 8 and handled with perturbative QCD, which is different from the collective approach employed in EPOS.

Unlike the EPOS sample, the PYTHIA 8 sample separates ND, SD and DD processes into three sub-samples. In order to preserve the correct ratio between cross sections of these processes, the sub-samples have to be weighted before they are combined, as shown in Table 4.1. The cross section values are based on calculations by PYTHIA and retrieved from the ATLAS Metadata Interface (AMI).

Chapter 5

Selection of K_s^0 and $\Lambda^0(\bar{\Lambda^0})$ candidates

The selections of events and candidates are inspired by other strange hadron analyses, such as [59], [60], and [61].

5.1 Event selection

Data events used in this analysis are required to pass the GRL selection, as discussed in Section 4.1. Further, data and MC events must each contain one primary vertex (PV) that is reconstructed with at least two tracks with $p_T > 100$ MeV, which is considered to be the point of pp collision. Pile-up events, defined as events containing one or more pile-up vertices that are reconstructed with four or more tracks, are removed to reduce background [62]. The number of events that survive each cut in the data and MC samples are shown in Tables 5.1 and 5.2, respectively.

5.2 V^0 reconstruction

The particles reconstructed in this analysis, K_s^0 and $\Lambda^0(\bar{\Lambda^0})$, are neutral particles that decay into a pair of oppositely charged particles, the tracks of which form a "V" shape - these

	Number of events	
Raw events	199,189,032	(100%)
Events in GRL	192,972,322	(96.9%)
Events with one PV	154,063,343	(77.3%)
Non pile-up events	151,784,918	(76.2%)
Events with $\geq 1 \ V^0$ candidate	136,515,953	(68.5%)

Table 5.1: Cut flow for data events.

	Pythia 8 ND	Pythia 8 SD	Pythia 8 DD	EPOS
Raw events	18,999,000	2,000,000	2,000,000	99,931,000
Events with one PV	18,902,752	1,083,318	1,174,987	83,080,176
Non pile-up events	18,897,041	1,083,215	1,174,916	83,044,373
Events with $\geq 1 \ V^0$ candidate	17,018,519	826,292	798,105	71,748,377

Table 5.2: Cut flow for MC events.

particles are hence called V^0 's. Their dominant decay channels and respective branching fractions are $K_s^0 \to \pi^+\pi^-(69.20 \pm 0.05\%)$ and $\Lambda^0 \to p\pi^-(\bar{\Lambda^0} \to \bar{p}\pi^+)(63.9 \pm 0.5\%)$ [63].

These decay channels are used for reconstruction in the InDetV0Finder package, which is a vertex finding algorithm combining all possible pairs of oppositely charged tracks in the ID and forming V^0 vertices. The V^0 candidates used in this analysis are required to be reconstructed with two tracks with $p_T > 100$ MeV and $|\eta| < 2.5$, and have a two-track vertex fit $\chi^2 < 15$.

The invariant mass of a V^0 candidate is given by:

$$m_{V^0} = \sqrt{(E_1 + E_2)^2 - |(\vec{p_1} + \vec{p_2})|^2}$$
(5.1)

where $E_{1,2}$ and $\vec{p_{1,2}}$ represent the energy and 3-momentum of the two track particles, respectively, used to reconstruct the V^0 candidate. The energy of a track particle is given by:

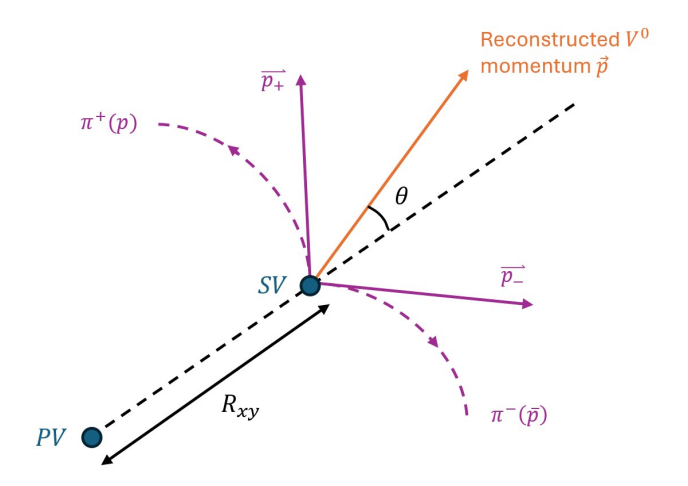


Figure 5.1: V^0 decay schematics

$$E_i = \sqrt{m_i^2 + |\vec{p_i}|^2}, \qquad i = 1, 2$$
 (5.2)

In this analysis, no particle identification is performed for track particles; therefore, each V^0 candidate is assigned K_s^0 , Λ^0 , and $\bar{\Lambda^0}$ invariant mass values using different track mass hypotheses. Explicitly, the K_s^0 invariant mass value is obtained by setting $m_1 = m_2 = m_{\pi^{\pm}}$; the Λ^0 and $\bar{\Lambda^0}$ invariant mass values are obtained by setting $m_1 = m_p$ and $m_2 = m_{\pi^{\pm}}$, with the track masses assigned according to their charges.

Selections are not applied in the InDetV0Finder tool but are applied on the outputs instead.

5.3 V^0 candidate selection

The kinematic variables of a V^0 decay are illustrated in Figure 5.1 and are defined as:

- θ : the pointing angle in 3D between the reconstructed V^0 momentum and the straight line connecting the PV and secondary vertex (SV)
- p_T : the transverse component of the reconstructed V^0 momentum (\vec{p})

• R_{xy} : the transverse distance between the PV and SV, which roughly corresponds to lifetime

The cut values are outlined in Table 5.3. The cut on θ is tighter for Λ^0 due to its larger backgrounds, while the minimum R_{xy} cut is higher for Λ^0 as it has a longer mean lifetime $((2.632 \pm 0.020) \times 10^{-10} \text{ s})$ than K_s^0 $((0.8954 \pm 0.0004) \times 10^{-10} \text{ s})$ [63]. Minimum p_T cuts are placed due to a larger number of fakes in the low- p_T regions, with a tighter cut used for Λ^0 as this effect is more extended over the p_T region compared to K_s^0 , as shown in [60]. The cuts on these three variables are shown in Figure 5.2.

Further cuts are placed on reconstructed mass values to remove candidates that fall within both K_s^0 and Λ^0 mass signal regions (defined in Section 5.4), and to remove excess in the low reconstructed K_s^0 mass region arising from e^+e^- events, as studied in [64]. These cuts are illustrated in Figure 5.3.

	K_s^0	$\Lambda^0(ar{\Lambda^0})$
$cos\theta$	> 0.9990	> 0.9998
$R_{xy} [\mathrm{mm}]$	4 - 450	17 - 450
$p_T [\mathrm{MeV}]$	> 300	> 500
K_s^0 invariant mass [MeV]	-	340 - 477 or $518 - 550$
Λ^0 invariant mass [MeV]	> 1123	-

Table 5.3: Selection cuts on V^0 candidates

5.4 Mass distributions

The distributions of the reconstructed K_s^0 , Λ^0 , and $\bar{\Lambda}^0$ masses of V^0 candidates in data passing the respective selections are presented in Figure 5.4. Each distribution is fitted with three functions, consisting of a Gaussian, double Gaussian, or non-relativistic Breit-Wigner signal function, on top of a 2nd-order polynomial background. The double Gaussian is

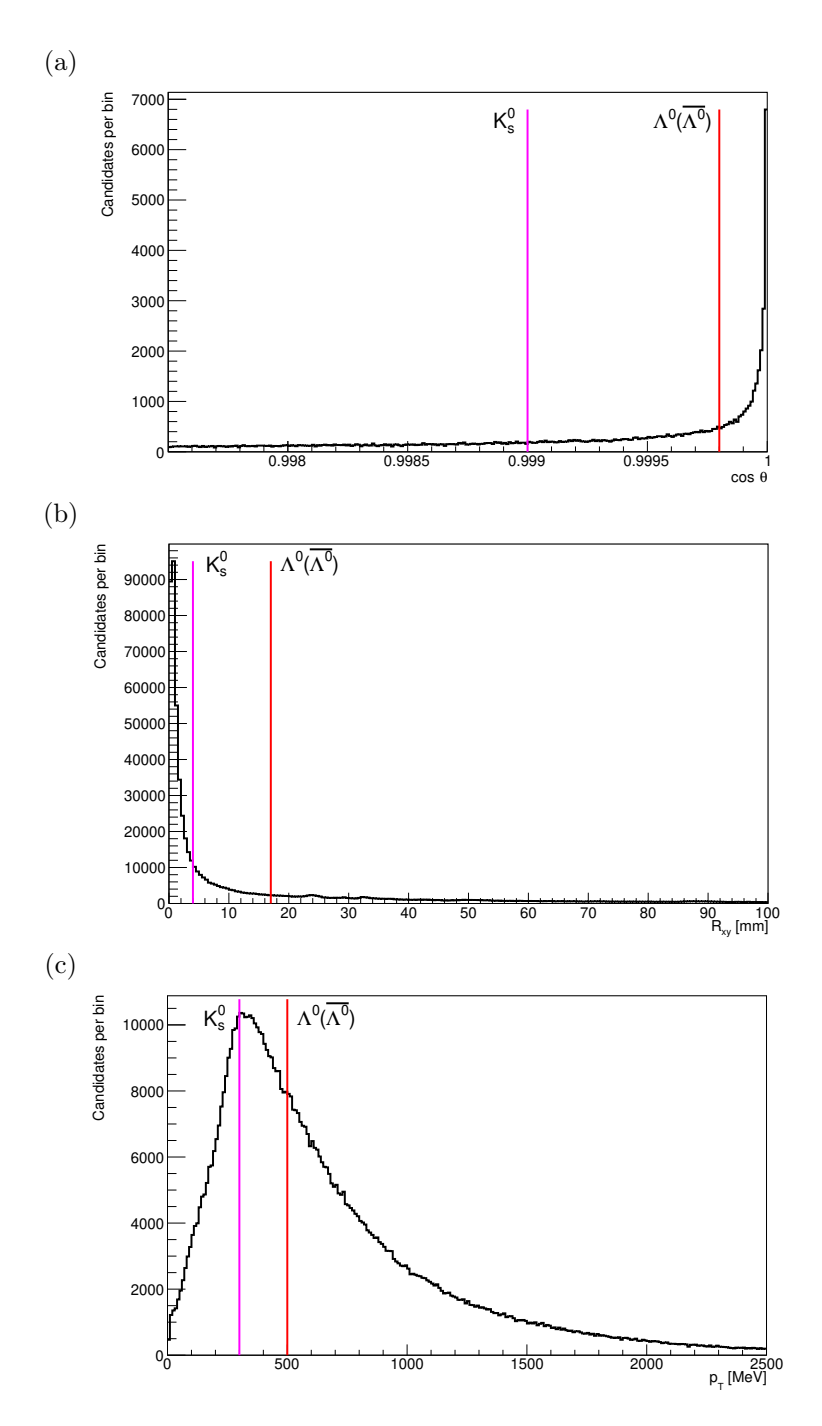


Figure 5.2: The distribution of V^0 candidates with respect to (a) $cos\theta$, (b) R_{xy} and (c) p_T . The vertical lines in magenta and red show the minimum cuts used to select K_s^0 and $\Lambda^0(\bar{\Lambda^0})$ candidates, respectively.

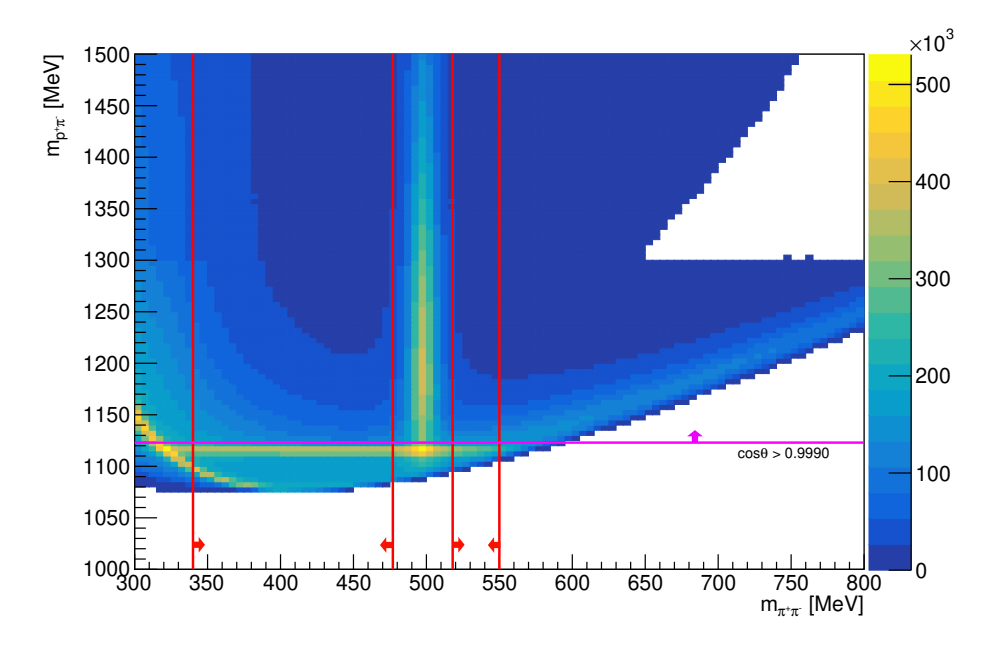


Figure 5.3: 2D histogram of reconstructed K_s^0 mass and Λ^0 mass. The lines and arrows in red (magenta) show cuts on the reconstructed K_s^0 (Λ^0) mass to select Λ^0 (K_s^0) candidates.

a sum of two Gaussian distributions with the same mean but different widths, while the non-relativistic Breit-Wigner distribution is given by:

$$f(x) = \frac{1}{2\pi} \cdot \frac{\Gamma}{(x - x_0)^2 + \Gamma^2/4}$$
 (5.3)

where x_0 is the median and Γ is the half-width at half-maximum of the distribution.

The goodness-of-fit is measured by the reduced chi-squared statistic (χ^2_{ν}) , which is related to chi-squared (χ^2) by:

$$\chi_{\nu}^2 = \chi^2 / n_{DOF} \tag{5.4}$$

where, for fitting a histogram, the number of degrees of freedom is given by:

$$n_{DOF} = \text{number of bins - number of free fit parameters} - 1$$
 (5.5)

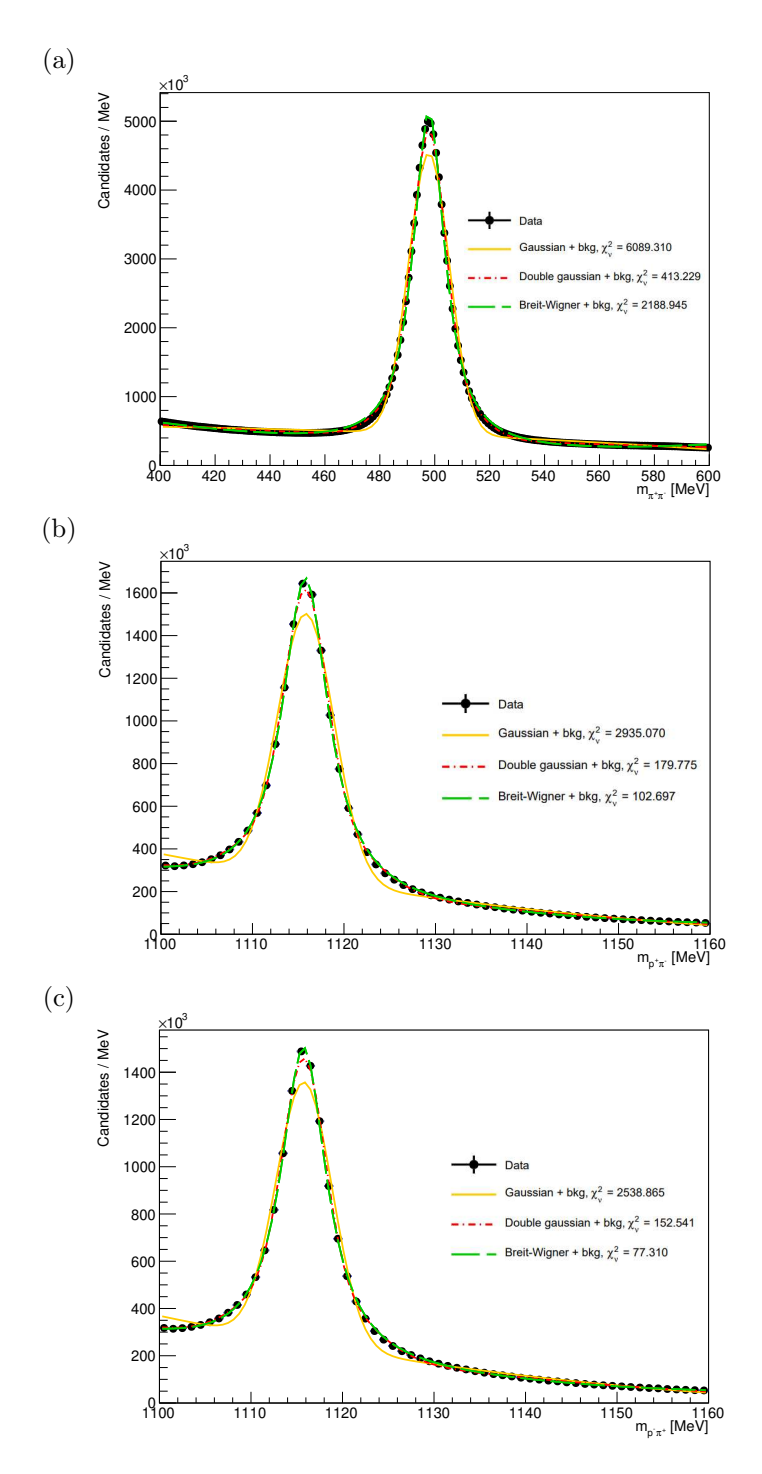


Figure 5.4: Mass distributions of (a) K^0_s , (b) Λ^0 and (c) $\bar{\Lambda^0}$ candidates in data, fitted with a Gaussian, double Gaussian, or non-relativistic Breit-Wigner signal on a 2nd order polynomial background.

The definition of the χ^2 statistic used here follows [65], where the histogram errors are assumed to be Poisson-distributed, which is appropriate for count data. The fit results are listed in Table 5.4 and show that the K_s^0 mass distribution is best described by the double Gaussian fit, and the Λ^0 and $\bar{\Lambda}^0$ mass distributions by the Breit-Wigner fit. Further, the fitted mass values are compared to the known Particle Data Group (PDG) values in Table 5.5, with the maximum difference between results from the three fit functions as an estimate of systematic errors. The statistical errors for all fitted mass values are $\approx 0.001 \text{MeV}$ and are hence negligible.

In this analysis, the single Gaussian fit parameter σ is used to roughly estimate the width of the mass peak, and the definition of signal regions of each particle type is taken to be approximately $\pm 3\sigma$ from the known mass values: for K_s^0 , we have $|m_{V^0} - m_{K_s^0, PDG}| < 20$ MeV, and for Λ^0 and $\bar{\Lambda}^0$, we have $|m_{V^0} - m_{\Lambda, PDG}| < 7$ MeV.

		K_s^0 mass	Λ^0 mass	$\bar{\Lambda^0}$ mass
Single Gaussian	μ	497.890	1115.86	1115.82
	σ	7.385	3.085	3.062
	$\chi^2_{ u}$	6089	2935	2539
Double Gaussian	μ	497.888	1115.82	1115.78
	σ_1	5.520	2.226	2.199
	σ_2	12.505	5.713	5.686
	C_1/C_2	2.971	2.725	2.677
	χ^2_{ν}	413	180	153
Breit-Wigner	x_0	497.892	1115.80	1115.76
	Γ	13.528	6.025	6.003
	$\chi^2_{ u}$	2189	103	77

Table 5.4: Fit parameters to mass distributions in data. For the double Gaussian fit, C_1/C_2 is the ratio between the amplitudes of the two Gaussians.

	Fitted mass [MeV]	PDG mass [MeV]
K_s^0	497.888 ± 0.004	497.611 ± 0.013
Λ^0	1115.80 ± 0.06	1115.683 ± 0.006
$ar{\Lambda^0}$	1115.76 ± 0.06	1115.683 ± 0.006

Table 5.5: Comparisons between fitted and PDG mass values [63]. The fitted values for K_s^0 are obtained from the double gaussian fit, and for Λ^0 and $\bar{\Lambda^0}$ from the Breit-Wigner fit.

5.5 Lifetime distributions

To further check that the applied cuts correctly select the desired species of V^0 particle, one can inspect the particle lifetime distributions and perform fits to extract their mean lifetime, as shown in Figure 5.5.

To obtain the lifetime τ of a particle, we first consider the general expression for the decay length d of a relativistic particle, given by:

$$d = \gamma v \tau = p\tau/m \tag{5.6}$$

and we have

$$\tau = \frac{dm}{p} \tag{5.7}$$

where v is the velocity of the particle, m is its mass (taken to be the PDG value), and p is the magnitude of its 3-momentum.

The lifetime distributions are then fitted with the function:

$$f(t) = C_0 + C_{bkg}e^{-t/\tau_{bkg}} + C_{sig}e^{-t/\tau_{sig}}$$
(5.8)

where the last term describes the contribution from the desired particle, or the signal, and the first two terms describe the background [66]. Assuming that the candidates passing selections are dominated by signal, as suggested by the clear peaks in invariant mass distributions in

Section 5.4, we impose $C_{sig} > C_{bkg}$ when fitting. The fit results along with the known mean lifetime values from PDG are presented in Table 5.6. As the analysis does not aim at making precise lifetime measurements, a simple assumption on the background profile is used and only statistical uncertainties are considered. Consequently, the fit results do not agree with the known values but are on the same order of magnitude, and this check is sufficient to show that the selected candidates indeed consist mostly of the desired particle species.

	K_s^0	Λ^0
$\tau_{sig} \ [10^{-10} \ \mathrm{s}]$	$0.6250 \pm 0.0009 (stat)$	$1.630 \pm 0.003 (\mathrm{stat})$
$\tau_{bkg} \ [10^{-10} \ {\rm s}]$	$3.438 \pm 0.006 (stat)$	$16.69 \pm 0.07 (\mathrm{stat})$
C_{sig}/C_{bkg}	$63.9 \pm 0.4 ({\rm stat})$	$19.7 \pm 0.1 (\mathrm{stat})$
PDG mean lifetime $[10^{-10} \text{ s}]$	0.8954 ± 0.0004	2.632 ± 0.020

Table 5.6: Fit results to lifetime distributions compared to the known mean lifetime values from PDG [63].

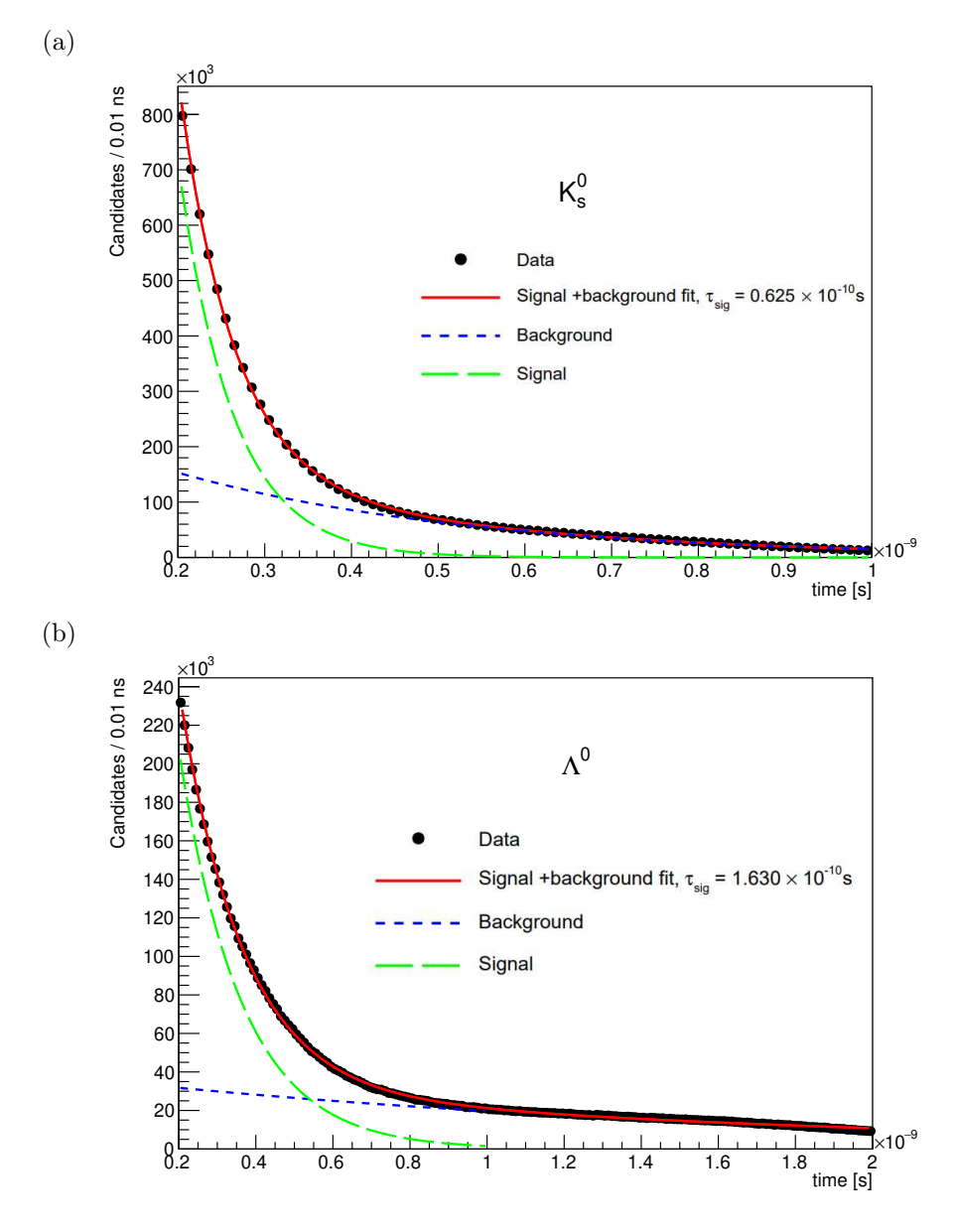


Figure 5.5: Lifetime distributions of (a) K_s^0 and (b) Λ^0 candidates in data, fitted with the signal plus background function described in Section 5.5.

Chapter 6

Results for K_s^0 and $\Lambda^0(\bar{\Lambda^0})$

6.1 Kinematic distributions

The K_s^0 and Λ^0 invariant mass distributions in data and MC are presented in Figure 6.1, with the MC distributions normalized to data by the number of candidates in the signal region, as defined in Section 5.4 and also indicated in the figure. The fit function that best describes each mass distribution in data is also shown.

The kinematic distributions of candidates in the signal regions are then studied. Figures 6.2 and 6.3 show the distributions of K_s^0 and Λ^0 signal candidates, respectively, in data and MC with respect to p_T , η and ϕ , where the MC distributions are again normalized to data. In addition, to better understand the separate contributions to the kinematic distributions from ND, SD and DD processes, the corresponding PYTHIA 8 subsamples are separately normalised to and compared with data, as shown in Figures 6.4 and 6.5.

Kinematic distributions for $\bar{\Lambda^0}$ are not separately shown, but instead are presented in Figure 6.6 as $\bar{\Lambda^0}/\Lambda^0$ production ratios with respect to the same kinematic variables. The overall $\bar{\Lambda^0}/\Lambda^0$ production ratios measured in data, predicted by EPOS and PYTHIA 8 are $0.909 \pm 0.001(\mathrm{stat}),~0.916 \pm 0.001(\mathrm{stat})$ and $0.922 \pm 0.002(\mathrm{stat})$, respectively. The higher

production rate of Λ^0 , made up of uds quarks, than its antiparticle in pp interactions is likely due to the fact that the proton contains u and d valence quarks that could be the ones contained inside the final state hadron.

As the detector and collision geometries are rotationally symmetric around the beamline, a flat distribution in ϕ is observed as expected.

Overall, EPOS agrees better with data in all p_T and η distributions. The PYTHIA 8 sample shows relative underproduction of strange hadrons in central pseudorapidity regions, which may be attributed to a lack of CD samples, as explained in Section 2.3.2, as well as relative overproduction at low p_T , which may be due to an overestimation of string fragmentation densities, leading to enhanced soft production.

6.2 Multiplicity distributions

The number of K_s^0 and $\Lambda^0(\bar{\Lambda^0})$ particles produced in each event, also known as multiplicity, is highly dependent on string fragmentation parameters (Section 2.4) and provides another test of different MC models. The comparisons between measured multiplicity distributions in data and predictions from the two MC models are shown in Figure 6.7.

For multiplicities of all three particles, EPOS shows slightly better agreement with data, but both MC models predict lower multiplicities than data, a phenomenon also seen for K_s^0 multiplicity in a similar analysis at $\sqrt{s} = 7$ TeV [59]. In general, the multiplicity of K_s^0 is higher than that of $\Lambda^0(\bar{\Lambda}^0)$ due to its lower mass.

6.3 Reconstruction efficiencies

For each MC sample, one can define the reconstruction efficiency ε for the physical object of interest (V^0 particles in this case) as the ratio between the number of such objects reconstructed and the number created at particle level, also known as truth level, in the same

phase space. We have:

$$\varepsilon = \frac{N_{reco}^{MC}}{N_{truth}^{MC}} \tag{6.1}$$

where N_{reco}^{MC} is the number of V^0 particles in MC that is reconstructed via the dominant decay mode such that it is consistent with reconstruction in data, and N_{truth}^{MC} is the number of V^0 's generated at truth level. In this analysis, the truth V^0 's are further required to decay via the dominant mode in order to avoid double counting caused by radiation processes for instance, $K_s^0 \to K_s^0 + gluon$ would be counted as two truth K_s^0 's. The reconstruction efficiency evaluated this way would be scaled up by a constant factor of the inverse of the branching ratio of the dominant decay mode, which would not affect the profile of differential production cross section measurements presented in Section 6.4.

The reconstruction efficiencies of K_s^0 , Λ^0 and $\bar{\Lambda}^0$ from the two MC models, with respect to the three kinematic variables, are presented in Figures 6.8, 6.9 and 6.10 respectively. For Λ^0 and $\bar{\Lambda}^0$, PYTHIA 8 gives lower overall reconstruction efficiencies than EPOS, as evident from the ϕ plots, but the opposite is shown in the p_T plots. This discrepancy is due to a significantly higher number of low- p_T truth particles generated in PYTHIA 8 than in EPOS, thus lowering the average efficiency because Λ^0 and $\bar{\Lambda}^0$ candidates with $p_T < 500$ MeV are not selected.

6.4 Cross section measurements

In general, cross section measurements are related to the number of reconstructed signal events in data (N_{sig}) by:

$$\sigma = \frac{N_{sig}}{L_{int} \cdot \varepsilon} \tag{6.2}$$

where L_{int} is the integrated luminosity and ε is the reconstruction efficiency.

As the reconstruction efficiencies are very low in the forward rapidity regions due to the limited coverage by the ID ($|\eta| < 2.5$), the inclusive production cross section measurements are susceptible to large uncertainties. Instead, in this analysis, the differential cross sections with respect to p_T , η and ϕ are studied and comparisons are made between K_s^0 , Λ^0 and $\bar{\Lambda}^0$, as shown in Figure 6.11. The procedure of obtaining the true differential cross sections from the measured distributions is called unfolding. In this analysis, this is performed by dividing the kinematic distributions measured in data by the binned reconstruction efficiencies. The efficiencies from the EPOS sample are used for unfolding as it has better agreement with the kinematic distributions measured in data than the PYTHIA 8 sample. Moreover, the effects of trigger selection on the scaling of cross sections are not explored in this thesis due to time constraints, and results in this work are only presented in arbitrary units.

As discussed in Section 6.3, the reconstruction efficiencies have been scaled by constant factors related to the branching ratios of the dominant decay modes, which does not affect the shape of individual curves shown in Figure 6.11. However, since the branching ratios are different between K_s^0 and $\Lambda^0(\bar{\Lambda}^0)$ (by $\approx 8\%$), the curves are scaled accordingly in order to accurately reflect the relative production rates of the three particles.

Overall, the production cross section of K_s^0 is higher than that of Λ^0 and $\bar{\Lambda}^0$ due to their mass differences. As expected, the production cross section of Λ^0 is higher than that of $\bar{\Lambda}^0$ and the reason is discussed in Section 6.1, and the ratio between these two particles is relatively constant over all three kinematic variables, which is in good agreement with other strange analyses such as [59].

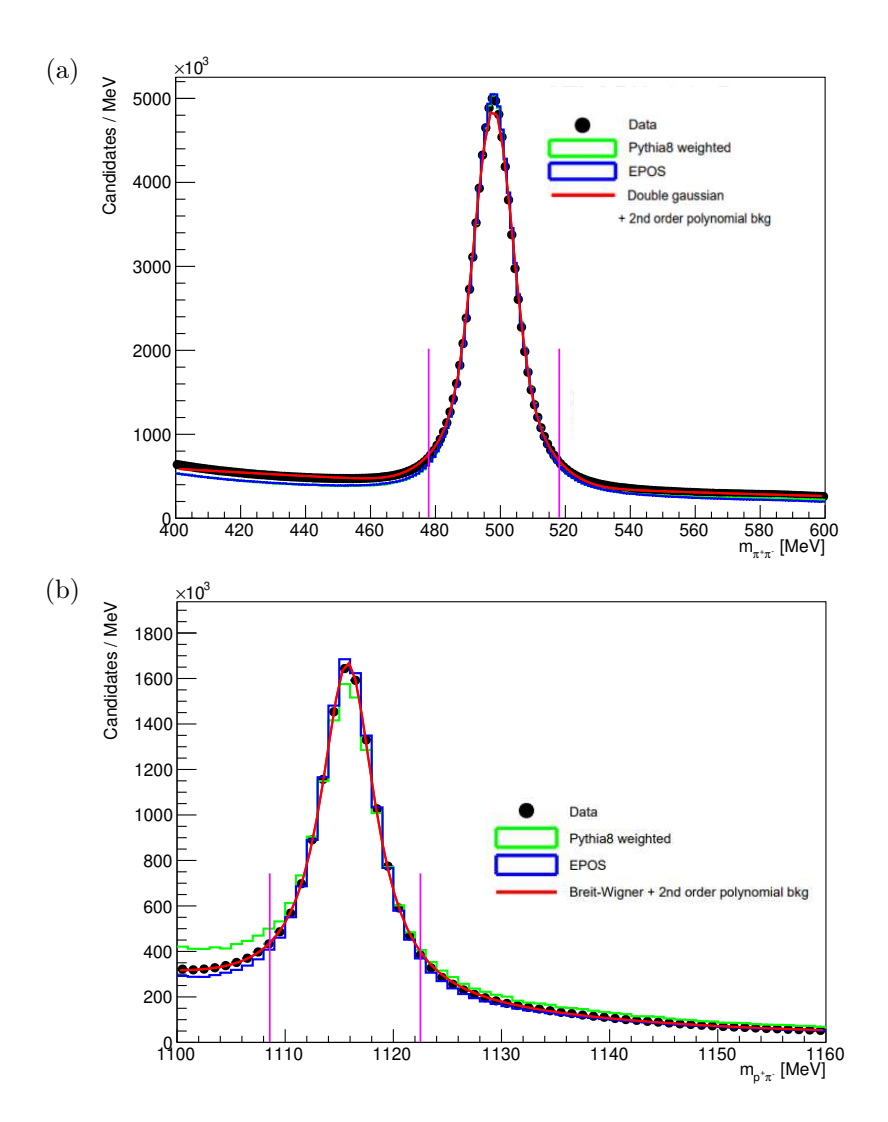


Figure 6.1: Distributions of (a) K_s^0 and (b) Λ^0 invariant masses in data and MC, with fitting performed on data as shown by the solid red line. MC histograms are normalized to data in the signal region, which is indicated by pairs of solid magenta lines.

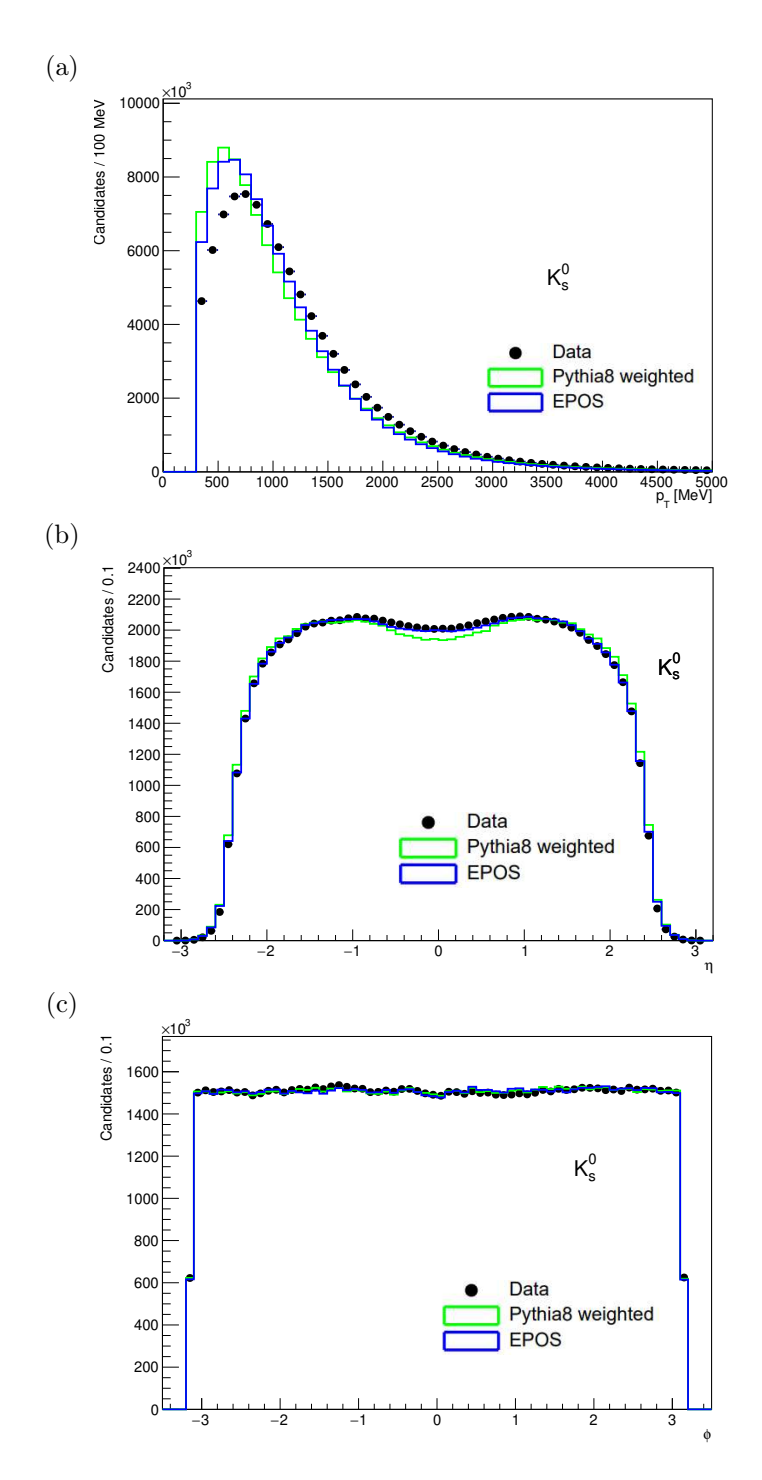


Figure 6.2: Kinematic distributions of K_s^0 candidates in data and MC with respect to (a) p_T , (b) η and (c) ϕ .MC histograms are normalized to data.

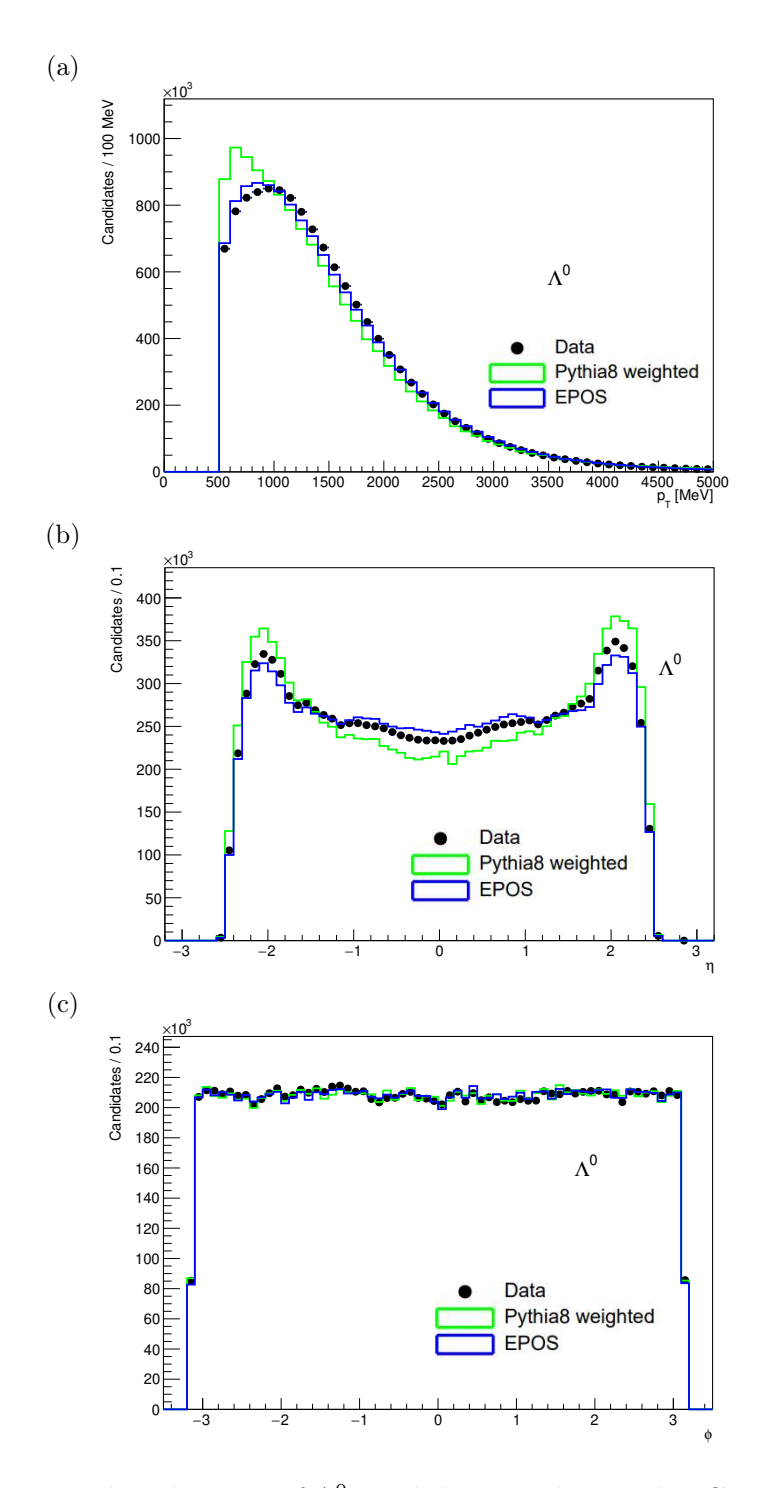


Figure 6.3: Kinematic distributions of Λ^0 candidates in data and MC with respect to (a) p_T , (b) η and (c) ϕ .MC histograms are normalized to data.

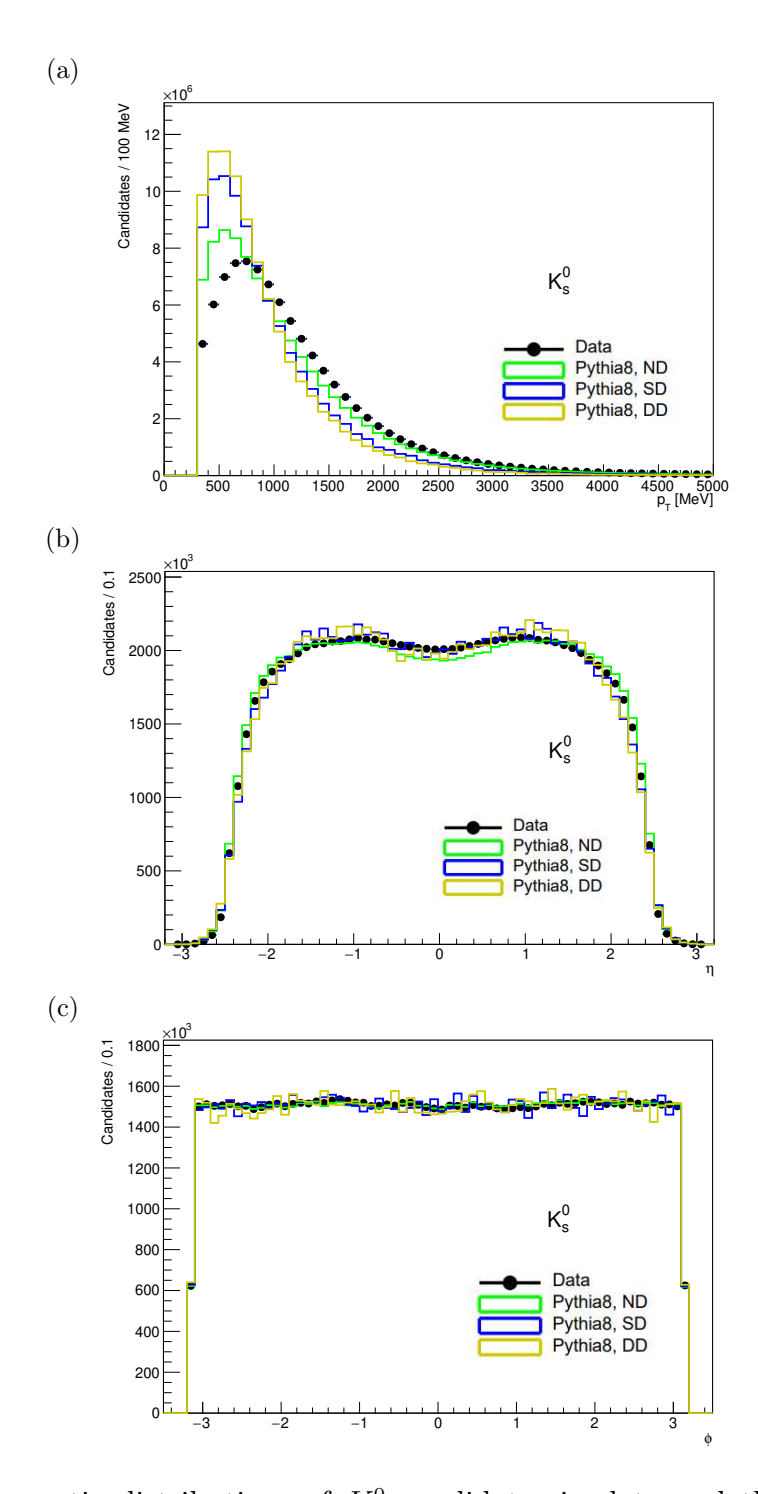


Figure 6.4: Kinematic distributions of K_s^0 candidates in data and the ND, SD and DD subsamples from PYTHIA 8, with respect to (a) p_T , (b) η and (c) ϕ . The PYTHIA 8 subsample histograms are separately normalized to data.

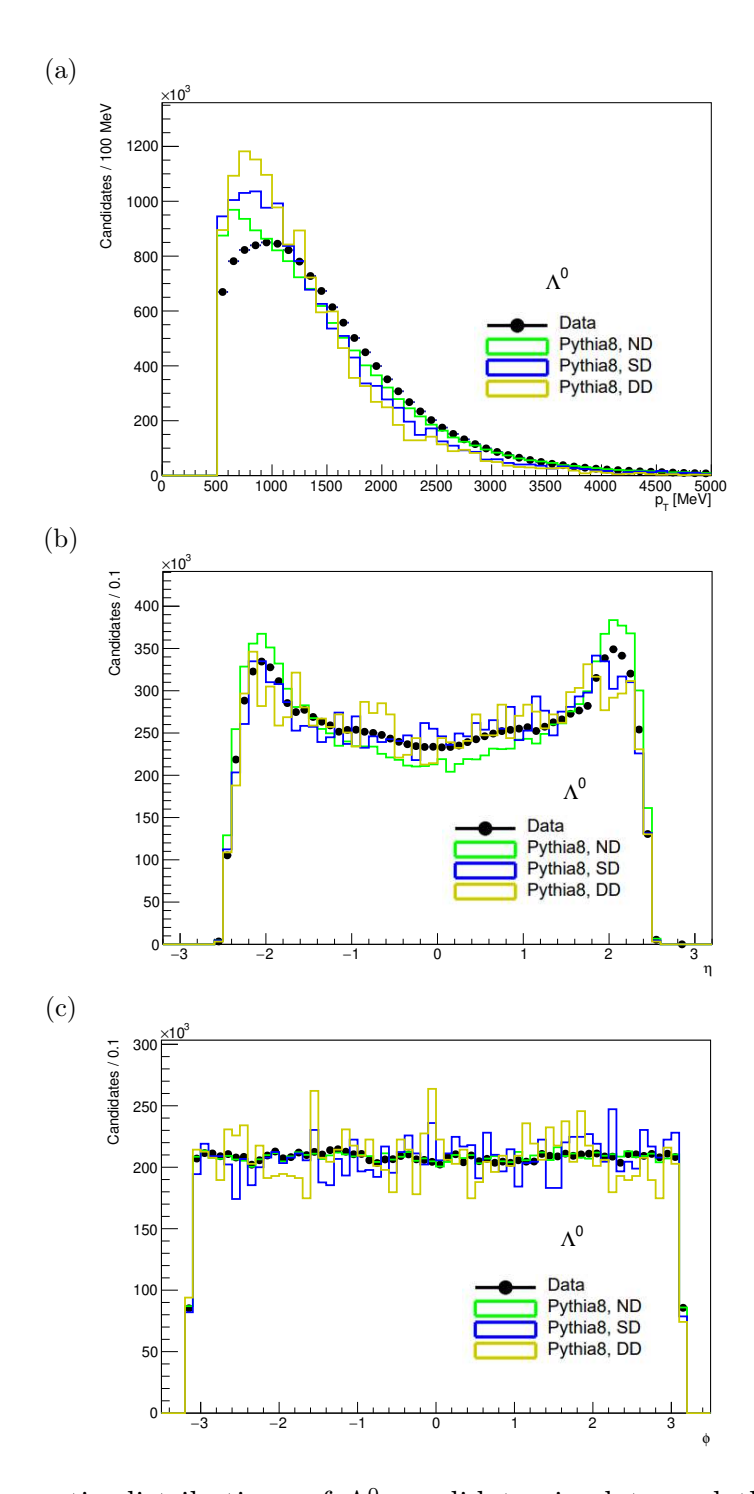


Figure 6.5: Kinematic distributions of Λ^0 candidates in data and the ND, SD and DD subsamples from PYTHIA 8, with respect to (a) p_T , (b) η and (c) ϕ . The PYTHIA 8 subsample histograms are separately normalized to data.

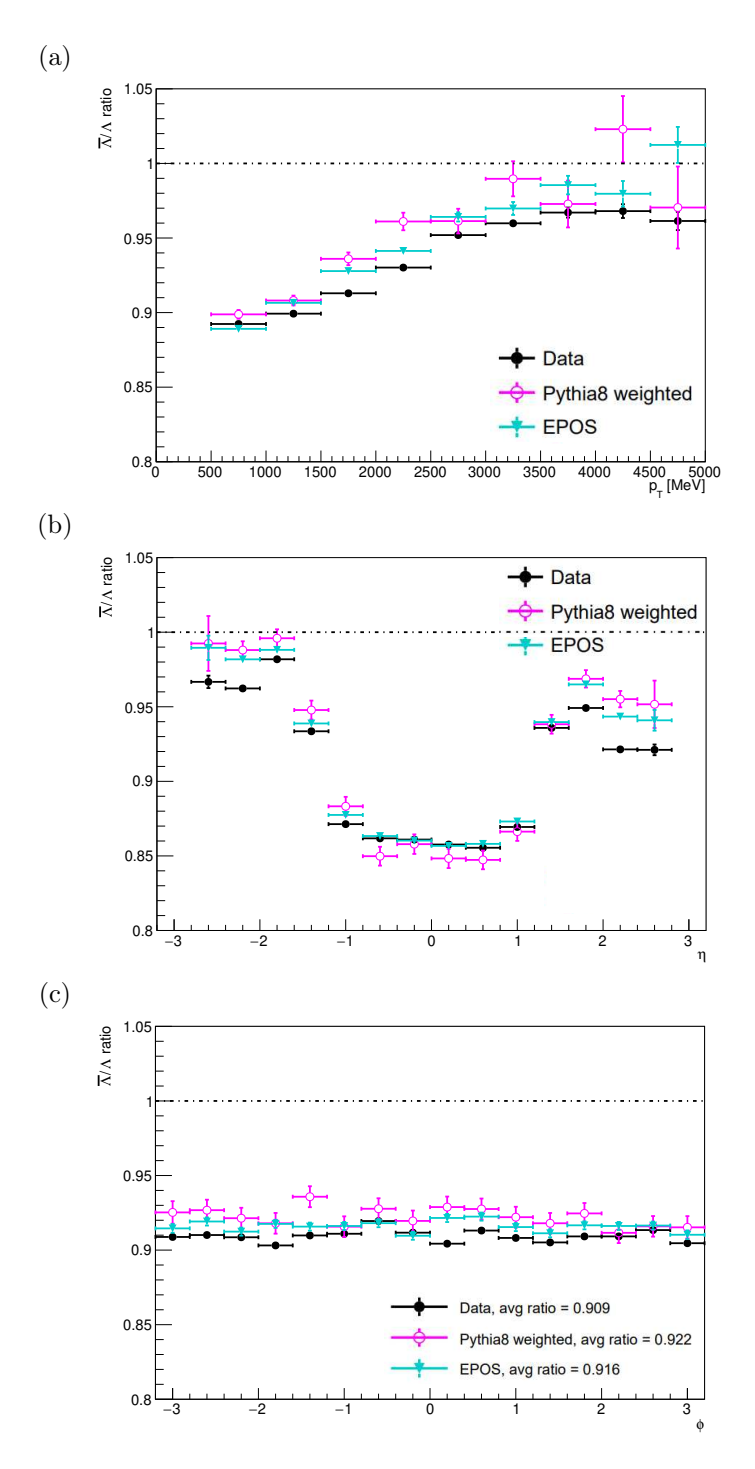


Figure 6.6: $\bar{\Lambda}^0/\Lambda^0$ production ratios in data and MC with respect to (a) p_T , (b) η and (c) ϕ . Only statistical uncertainties are shown.

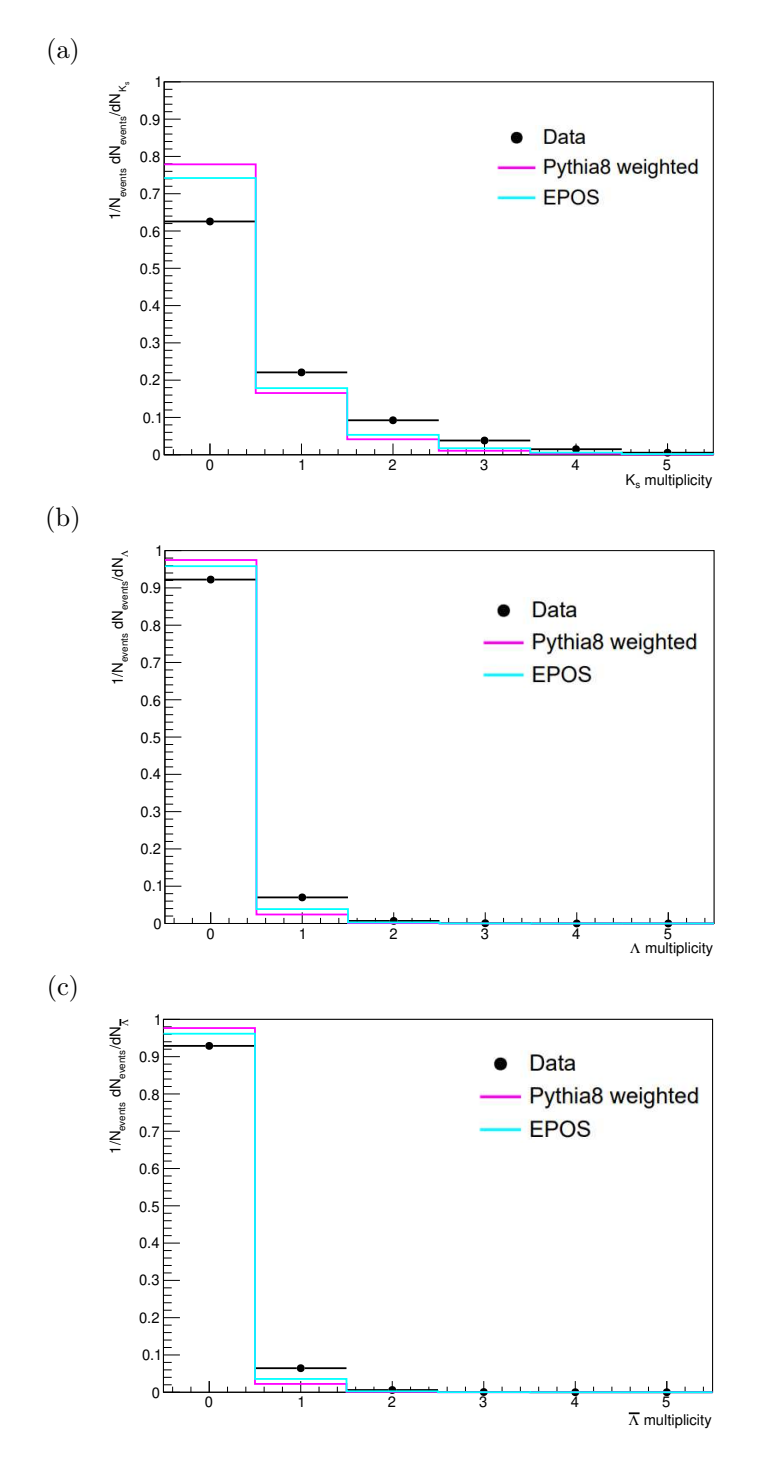


Figure 6.7: Particle multiplicity distributions of (a) K_s^0 , (b) Λ^0 and (c) $\bar{\Lambda^0}$ in data and MC, normalized to unity.

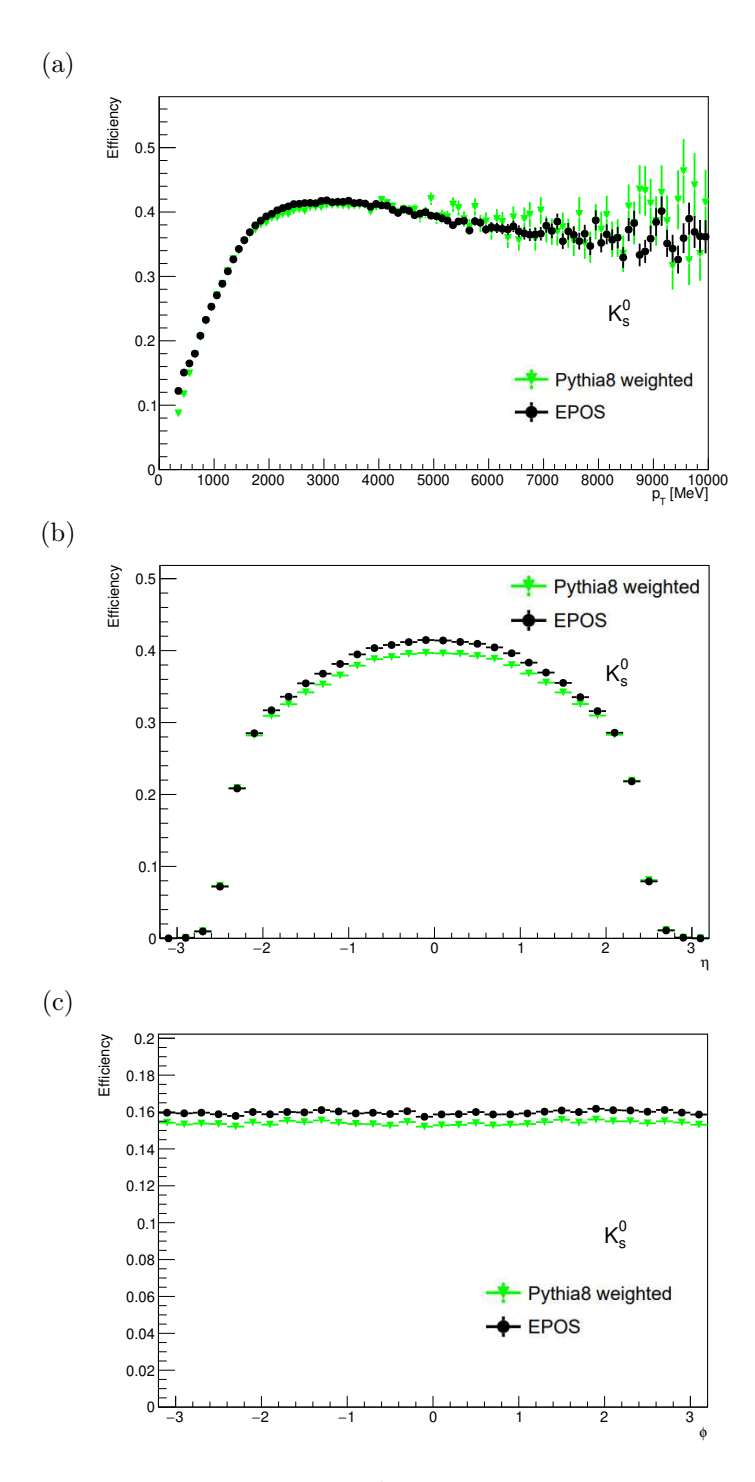


Figure 6.8: Reconstruction efficiencies of K_s^0 from the two MC models used, with respect to (a) p_T , (b) η and (c) ϕ . Only truth K_s^0 's decaying via $K_s^0 \to \pi^+\pi^-$ are considered. Only statistical uncertainties are shown.

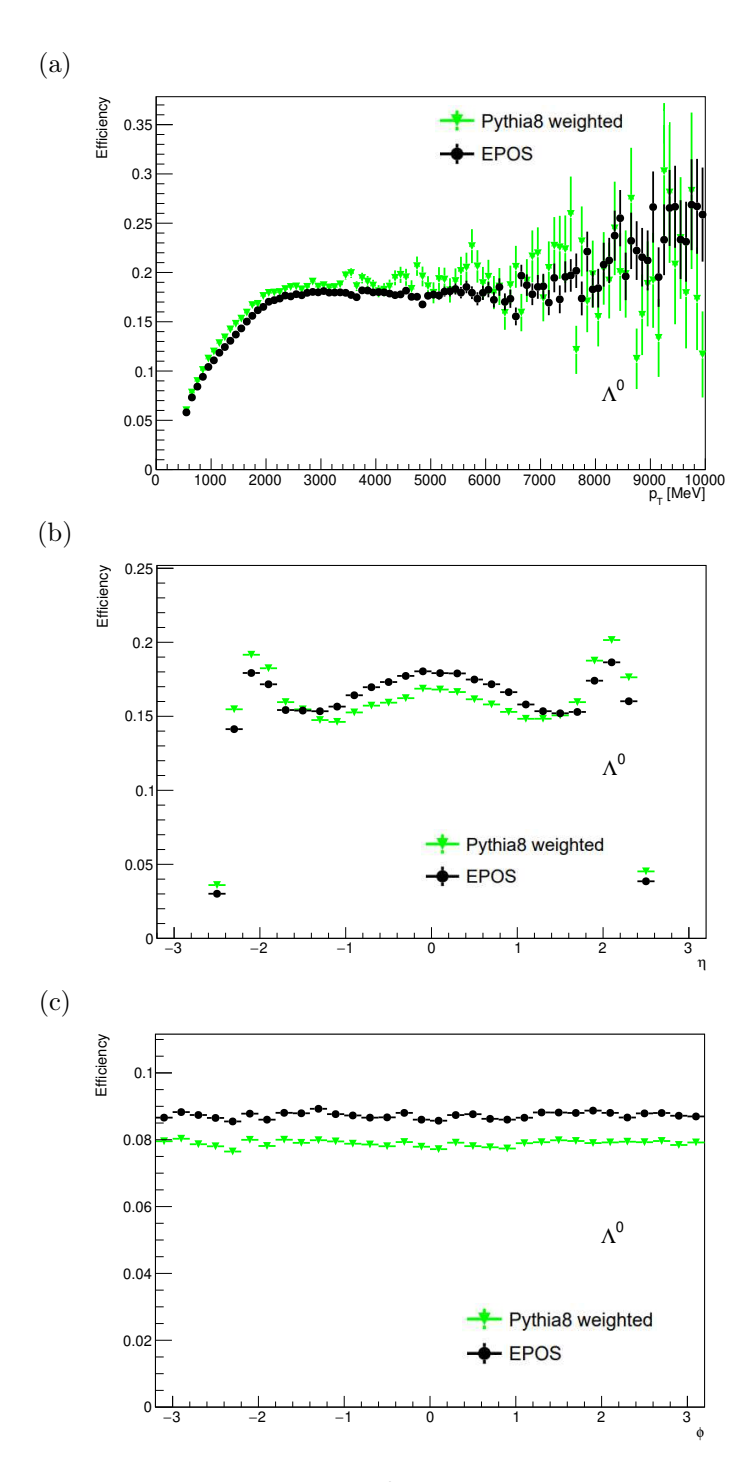


Figure 6.9: Reconstruction efficiencies of Λ^0 from the two MC models used, with respect to (a) p_T , (b) η and (c) ϕ . Only truth Λ^0 's decaying via $\Lambda^0 \to p\pi^-$ are considered. Only statistical uncertainties are shown.

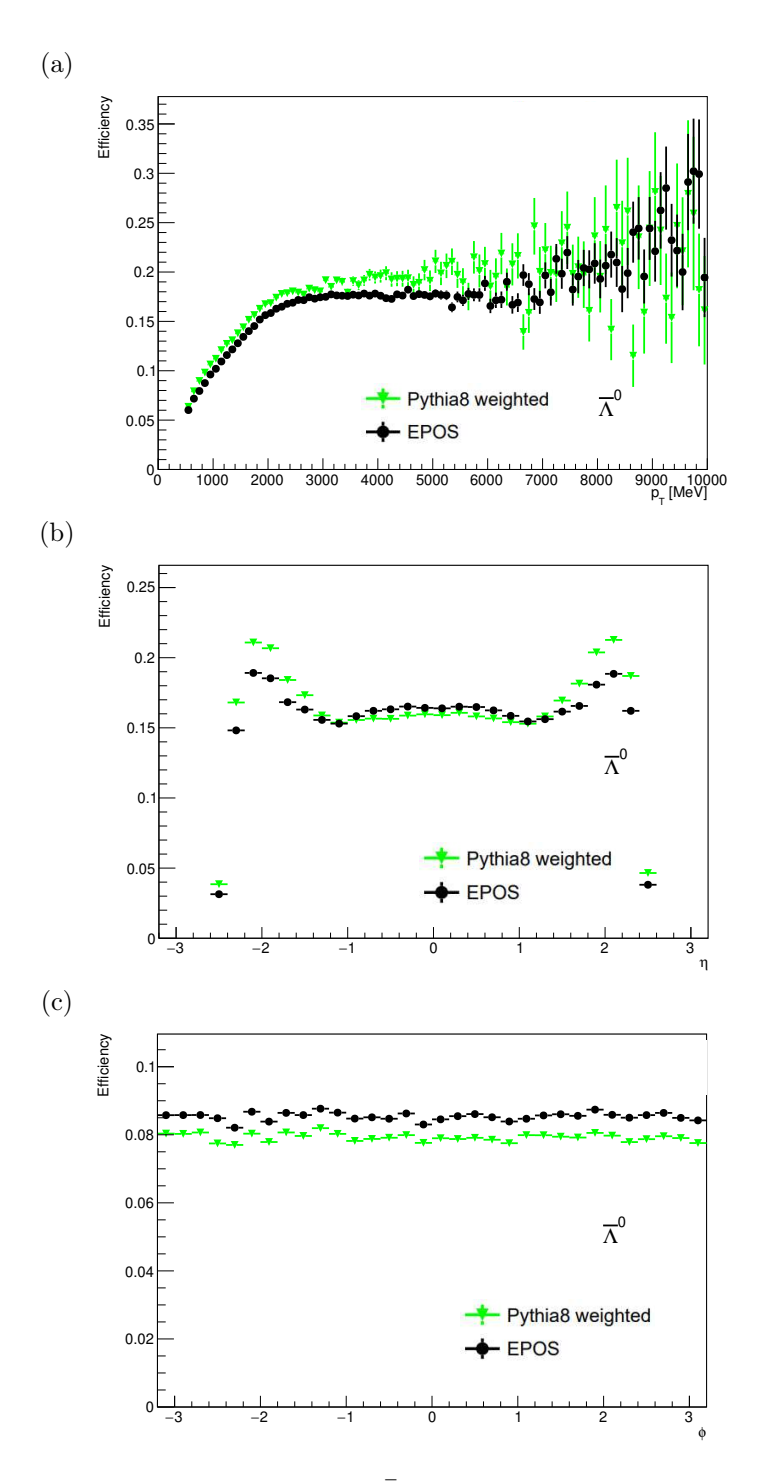


Figure 6.10: Reconstruction efficiencies of $\bar{\Lambda}^0$ from the two MC models used, with respect to (a) p_T , (b) η and (c) ϕ . Only truth $\bar{\Lambda}^0$'s decaying via $\bar{\Lambda}^0 \to \bar{p}\pi^+$ are considered. Only statistical uncertainties are shown.

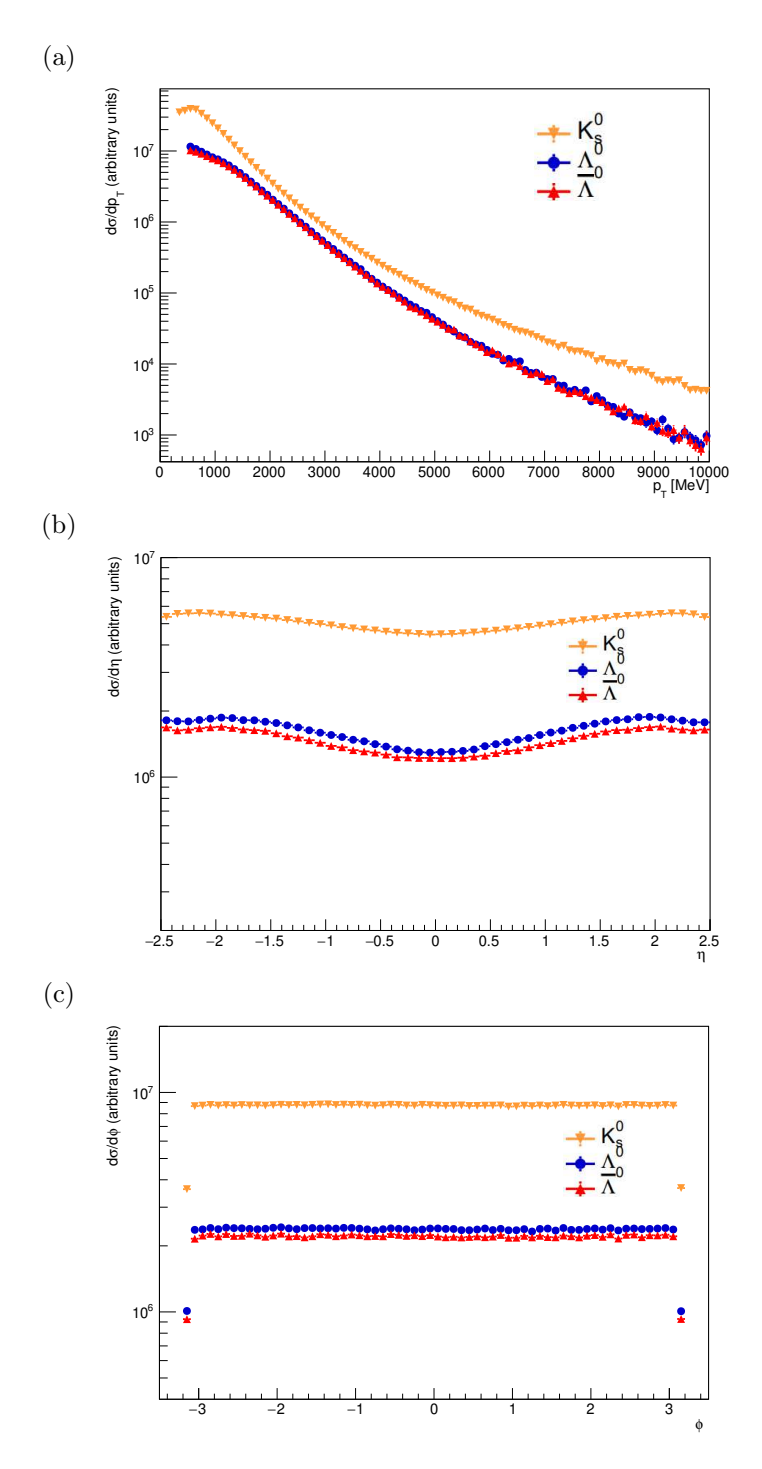


Figure 6.11: Differential production cross section for K_s^0 , Λ^0 and $\bar{\Lambda^0}$ in arbitrary units, with respect to (a) p_T , (b) η and (c) ϕ . Only statistical uncertainties are shown.

Chapter 7

Conclusion and outlook

In this work, strangeness production is studied by reconstructing the strange hadrons, K_s^0 , Λ^0 and $\bar{\Lambda}^0$, using minimum bias data from pp collisions at $\sqrt{s}=13$ TeV recorded by the ATLAS detector, which corresponds to an integrated luminosity of 13.65 nb⁻¹. Two MC samples, based on different hadronization models and handling of soft and hard processes, are also used. The particles of interest are reconstructed by a dedicated algorithm combining pairs of oppositely charged tracks in the inner detector. The candidates are passed through different sets of selection cuts on kinematic variables to select the desired type of particle with good purity, as demonstrated by invariant mass and lifetime distributions.

The yield distributions of the strange hadrons with respect to three kinematic variables $(p_T, \eta \text{ and } \phi)$ and their event multiplicities are presented with comparisons between data and MC, which show similar general profiles but also apparent discrepancies for certain distributions. Overall, EPOS MC shows better agreement with data than PYTHIA 8 MC, suggesting a more adequate phenomenological description of strangeness production.

The reconstruction efficiencies of strange hadrons in the two MC samples with respect to the same kinematic variables are presented. The profiles of differential production cross sections of the three particles are obtained by simple unfolding of data results, and the binned reconstruction efficiencies from the EPOS sample are used as they agree with data better. Further investigation into the effects of different trigger selections is needed to evaluate absolute cross section measurements.

Systematic uncertainties can be evaluated in future studies, which would improve the conclusiveness of the level of discrepancy between MC predictions and data results.

The analysis presented in this thesis can also be extended to other strange hadrons. One example is Ξ^- , which is a doubly strange particle with dominant decay mode $\Xi^- \to \Lambda^0 \pi^-$. It is expected to have a lower yield due to its higher mass and strangeness content but may be more sensitive to differences in modelling of strangeness production mechanisms in different MC samples. Attempts were made to reconstruct this particle by combining a signal Λ^0 with a charged track, but the lack of explicit track trajectories posed an obstacle to performing vertex fits, resulting in large backgrounds. This work also exceeded the time scope of this thesis.

In conclusion, this thesis presents measurements of strange hadron production in pp collisions, providing a sensitive probe into the strangeness content and fragmentation models of the proton.

List of Abbreviations

AMI ATLAS Metadata Interface

CD central diffractive

CSC cathode-strip chamber

DD double diffractive

GRL Good Runs List

HLT high level trigger

IBL insertable B-layer

ID Inner Detector

L1 Level-1

LAr liquid argon

LHC Large Hadron Collider

Linac4 Linear accelerator 4

MBTS Minimum Bias Trigger Scintillators

MC Monte Carlo

MDT monitored drift tube

MM Micromegas

MS Muon Spectrometer

ND non-diffractive

NSW New Small Wheel

CHAPTER 7. CONCLUSION AND OUTLOOK

PDF parton distribution function

PDG Particle Data Group

PS Proton Synchrotron

PSB Proton Synchrotron Booster

PV primary vertex

QCD Quantum chromodynamics

RF Radio Frequency

ROI Region-of-Interest

RPC Resistive Plate Chamber

SCT silicon microstrip detector

SD single diffractive

SM Standard Model

SPS Super Proton Synchrotron

sTGC small strips Thin Gap Chambers

SV secondary vertex

TGC Thin Gap Chamber

TRT transition radiation tracker

References

- [1] Cliff Burgess and Guy Moore. *The Standard Model: A Primer*. Cambridge University Press, 2006.
- [2] M.E. Peskin and D.V. Schroeder. An Introduction To Quantum Field Theory. Frontiers in Physics. Avalon Publishing, 1995. ISBN: 9780201503975. URL: https://books. google.ca/books?id=GjGy0AEACAAJ.
- [3] Wikimedia Commons. Standard Model of Elementary Particles. Original image by MissMJ, distributed under the Creative Commons Attribution 3.0 Unported license. 2008. URL: https://commons.wikimedia.org/wiki/File:Standard_Model_of_Elementary_Particles.svg.
- [4] ATLAS Collaboration. "Observation of a new particle in the search for the Standard Model Higgs boson with the ATLAS detector at the LHC". In: *Physics Letters B* 716.1 (Sept. 2012), pp. 1–29. ISSN: 0370-2693. DOI: 10.1016/j.physletb.2012.08.020. URL: http://dx.doi.org/10.1016/j.physletb.2012.08.020.
- [5] CMS Collaboration. "Observation of a new boson at a mass of 125 GeV with the CMS experiment at the LHC". In: Physics Letters B 716.1 (Sept. 2012), pp. 30-61. ISSN: 0370-2693. DOI: 10.1016/j.physletb.2012.08.021. URL: http://dx.doi.org/10.1016/j.physletb.2012.08.021.

- [6] Tim Gershon. "Overview of the Cabibbo-Kobayashi-Maskawa matrix". In: Pramana 79.5 (Nov. 2012), pp. 1091–1108. ISSN: 0973-7111. DOI: 10.1007/s12043-012-0418-y. URL: http://dx.doi.org/10.1007/s12043-012-0418-y.
- [7] Eugene Oks. "Brief review of recent advances in understanding dark matter and dark energy". In: New Astronomy Reviews 93 (Dec. 2021), p. 101632. ISSN: 1387-6473. DOI: 10.1016/j.newar.2021.101632. URL: http://dx.doi.org/10.1016/j.newar.2021.101632.
- [8] Thomas Hambye. "CP violation and the matter-antimatter asymmetry of the Universe". In: Comptes Rendus Physique 13.2 (Mar. 2012), pp. 193-203. ISSN: 1631-0705. URL: https://www.sciencedirect.com/science/article/pii/S1631070511001873.
- [9] B. Ananthanarayan and Ritesh K. Singh. "Direct observation of neutrino oscillations at the Sudbury Neutrino Observatory". In: Resonance 7.10 (Oct. 2002), pp. 79–82. ISSN: 0973-712X. DOI: 10.1007/BF02835546. URL: https://doi.org/10.1007/BF02835546.
- [10] S. Navas et al. "Review of Particle Physics". In: Phys. Rev. D 110 (3 Aug. 2024),
 p. 030001. DOI: 10.1103/PhysRevD.110.030001. URL: https://link.aps.org/doi/10.1103/PhysRevD.110.030001.
- [11] Kenneth G. Wilson. "Confinement of quarks". In: Phys. Rev. D 10 (8 Oct. 1974), pp. 2445-2459. DOI: 10.1103/PhysRevD.10.2445. URL: https://link.aps.org/doi/10.1103/PhysRevD.10.2445.
- [12] Zoltan Fodor and Christian Hoelbling. "Light hadron masses from lattice QCD". In: Reviews of Modern Physics 84.2 (Apr. 2012), pp. 449-495. ISSN: 1539-0756. DOI: 10. 1103/revmodphys.84.449. URL: http://dx.doi.org/10.1103/RevModPhys.84.449.

- [13] T Gehrmann, R G Roberts, and M R Whalley. "A compilation of structure functions in deep inelastic scattering". In: Journal of Physics G: Nuclear and Particle Physics 25.12A (Dec. 1999), A1. DOI: 10.1088/0954-3899/25/12A/301. URL: https://dx.doi.org/10.1088/0954-3899/25/12A/301.
- [14] Alan D. Martin. Proton structure, Partons, QCD, DGLAP and beyond. 2008. arXiv: 0802.0161 [hep-ph]. URL: https://arxiv.org/abs/0802.0161.
- [15] A. D. Martin et al. "Parton distributions for the LHC". In: The European Physical Journal C 63.2 (Sept. 2009), pp. 189–285. ISSN: 1434-6052. DOI: 10.1140/epjc/ s10052-009-1072-5. URL: https://doi.org/10.1140/epjc/s10052-009-1072-5.
- [16] A. Metz and A. Vossen. "Parton fragmentation functions". In: Progress in Particle and Nuclear Physics 91 (Nov. 2016), pp. 136–202. ISSN: 0146-6410. DOI: 10.1016/j.ppnp. 2016.08.003. URL: http://dx.doi.org/10.1016/j.ppnp.2016.08.003.
- [17] B. Andersson et al. "Parton fragmentation and string dynamics". In: *Physics Reports* 97.2 (1983), pp. 31–145. ISSN: 0370-1573. DOI: https://doi.org/10.1016/0370-1573(83)90080-7. URL: https://www.sciencedirect.com/science/article/pii/0370157383900807.
- [18] Torbjörn Sjöstrand et al. "An introduction to PYTHIA 8.2". In: Computer Physics Communications 191 (June 2015), pp. 159–177. ISSN: 0010-4655. DOI: 10.1016/j.cpc.2015.01.024. URL: http://dx.doi.org/10.1016/j.cpc.2015.01.024.
- [19] M. Deile. Diffraction and Total Cross-Section at the Tevatron and the LHC. 2006. arXiv: hep-ex/0602021 [hep-ex]. URL: https://arxiv.org/abs/hep-ex/0602021.
- [20] P. D. B. Collins. An Introduction to Regge Theory and High Energy Physics. Cambridge Monographs on Mathematical Physics. Cambridge University Press, July 2023. ISBN: 978-1-009-40326-9, 978-1-009-40329-0, 978-1-009-40328-3, 978-0-521-11035-8. DOI: 10. 1017/9781009403269.

- [21] E. Levin. Everything about reggeons. Part I:Reggeons in "soft" interaction. 1998. arXiv: hep-ph/9710546 [hep-ph]. URL: https://arxiv.org/abs/hep-ph/9710546.
- [22] Emily Nurse and Sercan Sen. "Large Rapidity Gap Method to Select Soft Diffraction Dissociation at the LHC". In: Advances in High Energy Physics 2016.1 (2016), p. 5082847. DOI: https://doi.org/10.1155/2016/5082847.
- [23] Sparsh Navin. Diffraction in Pythia. 2010. arXiv: 1005.3894 [hep-ph]. URL: https://arxiv.org/abs/1005.3894.
- [24] Gunnar Ingelman. Diffractive Hard Scattering. 1999. arXiv: hep-ph/9912534 [hep-ph].

 URL: https://arxiv.org/abs/hep-ph/9912534.
- [25] ALICE Collaboration. "Enhanced production of multi-strange hadrons in high-multiplicity proton-proton collisions". In: *Nature Physics* 13.6 (Apr. 2017), pp. 535–539. ISSN: 1745-2481. DOI: 10.1038/nphys4111. URL: http://dx.doi.org/10.1038/nphys4111.
- [26] Lyndon Evans and Philip Bryant. "LHC Machine". In: JINST 3 (2008), S08001. DOI: 10.1088/1748-0221/3/08/S08001.
- [27] CERN. CERN's accelerator complex. https://home.cern/science/accelerators/accelerator-complex.
- [28] The ATLAS Collaboration. "The ATLAS Experiment at the CERN Large Hadron Collider". In: Journal of Instrumentation 3.08 (Aug. 2008), S08003. DOI: 10.1088/ 1748-0221/3/08/S08003. URL: https://dx.doi.org/10.1088/1748-0221/3/08/ S08003.
- [29] CMS Collaboration. "The CMS Experiment at the CERN LHC". In: JINST 3 (2008),S08004. DOI: 10.1088/1748-0221/3/08/S08004.
- [30] LHCb Collaboration. "The LHCb Detector at the LHC". In: Journal of Instrumentation 3.08 (Aug. 2008), S08005. DOI: 10.1088/1748-0221/3/08/S08005. URL: https://dx.doi.org/10.1088/1748-0221/3/08/S08005.

- [31] ALICE Collaboration. "The ALICE experiment at the CERN LHC". In: *JINST* 3 (2008), S08002. DOI: 10.1088/1748-0221/3/08/S08002.
- [32] R Alemany-Fernandez et al. Operation and Configuration of the LHC in Run 1. Internal Note. 2013. URL: https://cds.cern.ch/record/1631030.
- [33] Jorg Wenninger. Operation and Configuration of the LHC in Run 2. Internal Note. 2019. URL: https://cds.cern.ch/record/2668326.
- [34] The ATLAS Collaboration. "The ATLAS experiment at the CERN Large Hadron Collider: a description of the detector configuration for Run 3". In: Journal of Instrumentation 19.05 (May 2024), P05063. ISSN: 1748-0221. DOI: 10.1088/1748-0221/19/05/p05063. URL: http://dx.doi.org/10.1088/1748-0221/19/05/p05063.
- [35] O. Aberle et al. High-Luminosity Large Hadron Collider (HL-LHC): Technical design report. CERN Yellow Reports: Monographs. Geneva: CERN, 2020. DOI: 10.23731/ CYRM-2020-0010. URL: https://cds.cern.ch/record/2749422.
- [36] The ATLAS Collaboration. "ATLAS magnet system: Technical design report". In: (Apr. 1997). URL: https://cds.cern.ch/record/338080.
- [37] Giulia Di Gregorio. "The Large Hadron Collider and the ATLAS Experiment". In: A Beauty-ful Boson: Search for the Higgs Boson Produced in Association with a Vector Boson and Decaying into a Pair of b-quarks Using Large-R Jets with the ATLAS Detector. Cham: Springer International Publishing, 2023, pp. 31–45. ISBN: 978-3-031-20013-7. DOI: 10.1007/978-3-031-20013-7_2. URL: https://doi.org/10.1007/978-3-031-20013-7_2.
- [38] The ATLAS Collaboration. Track Reconstruction Performance of the ATLAS Inner Detector at $\sqrt{s}=13~TeV$. Tech. rep. All figures including auxiliary figures are available at https://atlas.web.cern.ch/Atlas/GROUPS/PHYSICS/PUBNOTES/ATL-PHYS-PUB-2015-018. Geneva: CERN, 2015. URL: https://cds.cern.ch/record/2037683.

- [39] The ATLAS Collaboration. ATLAS inner detector: Technical Design Report, 1. Technical design report. ATLAS. Geneva: CERN, 1997. URL: https://cds.cern.ch/record/331063.
- [40] Devin James Mahon and ATLAS LAr Collaboration. ATLAS LAr Calorimeter Performance in LHC Run-2. Tech. rep. 06. Geneva: CERN, 2020. DOI: 10.1088/1748-0221/15/06/C06045. URL: https://cds.cern.ch/record/2715774.
- [41] ATLAS Collaboration. Operation and performance of the ATLAS tile calorimeter in LHC Run 2. 2024. arXiv: 2401.16034 [hep-ex]. URL: https://arxiv.org/abs/2401.16034.
- [42] Maria Perganti. New Small Wheels for the ATLAS Muon Spectrometer. Tech. rep. Geneva: CERN, 2020. URL: https://cds.cern.ch/record/2742986.
- [43] M. Nicolás Viaux. "The ATLAS 'New Small Wheel' Muon detector stations recently commissioned for LHC Run3". In: Nuclear Instruments and Methods in Physics Research Section A: Accelerators, Spectrometers, Detectors and Associated Equipment 1045 (2023), p. 167574. ISSN: 0168-9002. DOI: https://doi.org/10.1016/j.nima. 2022.167574. URL: https://www.sciencedirect.com/science/article/pii/S016890022200866X.
- [44] T Kawamoto et al. New Small Wheel Technical Design Report. Tech. rep. CERN, ATLAS Collaboration, 2013. URL: https://cds.cern.ch/record/1552862.
- [45] ATLAS Collaboration. "Operation of the ATLAS trigger system in Run 2". In: Journal of Instrumentation 15.10 (Oct. 2020), P10004–P10004. ISSN: 1748-0221. DOI: 10.1088/1748-0221/15/10/p10004. URL: http://dx.doi.org/10.1088/1748-0221/15/10/P10004.

- [46] ATLAS Collaboration. "Rapidity gap cross sections measured with the ATLAS detector in pp collisions at $\sqrt{s}=7$ TeV". In: The European Physical Journal C 72.3 (Mar. 2012). ISSN: 1434-6052. DOI: 10.1140/epjc/s10052-012-1926-0. URL: http://dx.doi.org/10.1140/epjc/s10052-012-1926-0.
- [47] ATLAS Collaboration. "Measurement of the inelastic proton–proton cross-section at $\sqrt{s}=7$ TeV with the ATLAS detector". In: *Nature Communications* 2.1 (Sept. 2011). ISSN: 2041-1723. DOI: 10.1038/ncomms1472. URL: http://dx.doi.org/10.1038/ncomms1472.
- [48] A. Sidoti. "Minimum Bias Trigger Scintillators in ATLAS Run II". In: Journal of Instrumentation 9.10 (Oct. 2014), p. C10020. DOI: 10.1088/1748-0221/9/10/C10020.
 URL: https://dx.doi.org/10.1088/1748-0221/9/10/C10020.
- [49] ATLAS Collaboration. Performance of the Minimum Bias Trigger in p-p Collisions at √s = 7 TeV. Tech. rep. All figures including auxiliary figures are available at https://atlas.web.cern.ch/Atlas/GROUPS/PHYSICS/CONFNOTES/ATLAS-CONF-2010-068. Geneva: CERN, 2010. URL: https://cds.cern.ch/record/1281343.
- [50] ATLAS Collaboration. Public ATLAS Luminosity Results for Run-2 of the LHC. https://twiki.cern.ch/twiki/bin/view/AtlasPublic/LuminosityPublicResultsRun2.
- [51] ATLAS Collaboration. "Luminosity determination in pp collisions at $\sqrt{s} = 13$ TeV using the ATLAS detector at the LHC". In: (2022). DOI: 10.48550/ARXIV.2212.09379. arXiv: 2212.09379 [hep-ex].
- [52] S. Porteboeuf, T. Pierog, and K. Werner. Producing Hard Processes Regarding the Complete Event: The EPOS Event Generator. 2010. arXiv: 1006.2967 [hep-ph]. URL: https://arxiv.org/abs/1006.2967.

- [53] T. Pierog and K. Werner. "EPOS Model and Ultra High Energy Cosmic Rays". In: Nuclear Physics B - Proceedings Supplements 196 (Dec. 2009), pp. 102-105. ISSN: 0920-5632. DOI: 10.1016/j.nuclphysbps.2009.09.017. URL: http://dx.doi.org/ 10.1016/j.nuclphysbps.2009.09.017.
- [54] T. Pierog et al. "EPOS LHC: Test of collective hadronization with data measured at the CERN Large Hadron Collider". In: *Physical Review C* 92.3 (Sept. 2015). ISSN: 1089-490X. DOI: 10.1103/physrevc.92.034906. URL: http://dx.doi.org/10.1103/PhysRevC.92.034906.
- [55] ATLAS Collaboration. Further ATLAS tunes of PYTHIA6 and Pythia 8. Tech. rep. Geneva: CERN, 2011. URL: https://cds.cern.ch/record/1400677.
- [56] S. Agostinelli et al. "Geant4—a simulation toolkit". In: Nuclear Instruments and Methods in Physics Research Section A: Accelerators, Spectrometers, Detectors and Associated Equipment 506.3 (2003), pp. 250–303. ISSN: 0168-9002. DOI: https://doi.org/10.1016/S0168-9002(03)01368-8. URL: https://www.sciencedirect.com/science/article/pii/S0168900203013688.
- [57] ATLAS Collaboration. "The ATLAS Simulation Infrastructure". In: The European Physical Journal C 70.3 (Dec. 2010), pp. 823-874. ISSN: 1434-6052. DOI: 10.1140/ epjc/s10052-010-1429-9. URL: https://doi.org/10.1140/epjc/s10052-010-1429-9.
- [58] H.J. Drescher et al. "Parton-based Gribov-Regge theory". In: Physics Reports 350.2-4
 (Sept. 2001), pp. 93-289. ISSN: 0370-1573. DOI: 10.1016/s0370-1573(00)00122-8.
 URL: http://dx.doi.org/10.1016/S0370-1573(00)00122-8.
- [59] ATLAS Collaboration. " K_s^0 and Λ production in pp interactions at $\sqrt{s} = 0.9$ and 7 TeV measured with the ATLAS detector at the LHC". In: *Phys. Rev. D* 85 (1 Jan.

- 2012), p. 012001. DOI: 10.1103/PhysRevD.85.012001. URL: https://link.aps.org/doi/10.1103/PhysRevD.85.012001.
- [60] ATLAS Collaboration. "Underlying-event studies with strange hadrons in pp collisions at $\sqrt{s} = 13$ TeV with the ATLAS detector". In: (2024). arXiv: 2405.05048 [hep-ex].
- [61] Antara Paul. Search for multiquark states decaying into neutral strange particles, kaons and lambdas, using the ATLAS detector. Master's thesis. McGill University, 2023.
- [62] ATLAS Collaboration. "Charged-particle multiplicities in pp interactions measured with the ATLAS detector at the LHC". In: New Journal of Physics 13.5 (May 2011), p. 053033. DOI: 10.1088/1367-2630/13/5/053033. URL: https://dx.doi.org/10.1088/1367-2630/13/5/053033.
- [63] Particle Data Group et al. "Review of Particle Physics". In: Progress of Theoretical and Experimental Physics 2022.8 (Aug. 2022), p. 083C01. ISSN: 2050-3911. DOI: 10.1093/ptep/ptac097. eprint: https://academic.oup.com/ptep/article-pdf/2022/8/083C01/49175539/ptac097.pdf. URL: https://doi.org/10.1093/ptep/ptac097.
- [64] Natalie Oosterman. Isolating e⁺e⁻ data from the background in search for multiquark decay into strange particles in the ATLAS detector. Summer Student Report. McGill University, Aug. 2022.
- [65] Steve Baker and Robert D. Cousins. "Clarification of the use of CHI-square and likelihood functions in fits to histograms". In: Nuclear Instruments and Methods in Physics Research 221.2 (1984), pp. 437–442. ISSN: 0167-5087. DOI: https://doi.org/10.1016/0167-5087(84)90016-4. URL: https://www.sciencedirect.com/science/article/pii/0167508784900164.
- [66] Sloane Sirota. Observation of Strange Particles and Strangeness Production at the Large Hadron Collider. Summer Student Report. McGill University, 2022.